Targeting type I regulatory T cells to enhance anti-parasitic T helper 1 and T follicular helper cell responses in human malaria

Running title: Tr1 cell modulation enhances Th1 and Tfh cells in malaria

Luzia Bukali[1,2*], Jessica A. Engel[1,*], Damian Oyong[3,*], Fabian de Labastida Rivera[1], Megan Soon[3], Dean Andrew[1], Nicholas L. Dooley[3], Mayimuna Nalubega[2,3], Reena Mukhiya[3,4], Teija M. Frame[1,2], Julianne Hamelink[2,3], Jessica R. Loughland[1,3], Rebecca Webster[1], Fiona Amante[1], Timothy N.C. Wells[5], Stephan Chalon[5], Joerg J. Moehrle[5,6,7], James S. McCarthy[8], Michael D. Leipold[9], Gerlinde Obermoser[9], Holden T. Maecker[9], Bridget E Barber[1,11,12,#], Michelle J. Boyle[3,#] and Christian R. Engwerda[1,#]

Author Affiliations:

1. QIMR Berghofer, Brisbane, QLD, Australia
2. University of Queensland, Brisbane, QLD, Australia
3. Burnet Institute, Melbourne, VIC, Australia
4. Griffith University, Brisbane, Australia
5. Medicines for Malaria Venture, Geneva, Switzerland
6. University of Basel, Basel, Switzerland
7. Swiss Tropical and Public Health Institute, Allschwil, Switzerland
8. Department of Infectious Diseases, The University of Melbourne Peter Doherty Institute for Infection and Immunity, Melbourne, Victoria, Australia
9. Stanford University, Stanford, CA, USA
10. Australian Defence Force Malaria and Infectious Disease Institute, Brisbane, QLD, Australia
11. Royal Brisbane & Women's Hospital, Brisbane, QLD, Australia
12. Menzies School of Health Research, Darwin, NT, Australia

* These authors contributed equally to this work

\# These authors contributed equally to this work

Abstract (200 words)

Type I interferon (IFN) signalling promotes development of type 1 regulatory (Tr1) $CD4^+$ T cells, which suppress inflammation but may limit protective immunity in malaria by constraining effector Th1 cells and antibody-promoting T follicular helper (Tfh) cells. We tested whether transiently blocking IFN-driven JAK/STAT signalling with ruxolitinib would reduce Tr1 cell development and enhance protective Th1 and Tfh cell responses. Using controlled human malaria infection, we investigated the impact of ruxolitinib on $CD4^+$ T cell activation and antigen-specific immunity. Whole blood stimulation with IFNβ, IL-2, or PMA/Ionomycin revealed that ruxolitinib suppressed pSTAT1, pSTAT3, and pSTAT5 in $CD4^+$ T cells following treatment. However, antigen-specific $CD4^+$ T cell responses were preserved. Further, ruxolitinib enhanced recall $CD4^+$ T cell responses during a second infection, with increased frequencies of antigen-specific Th1, Tfh, and Tr1 cell subsets. Transcriptional analysis revealed overlapping gene signatures and clonal sharing between Th1, Tfh and Tr1 cells. These findings show transient JAK inhibition can modulate development of Th1, Tfh and Tr1 cell subsets in malaria, suppressing inhibitory signalling while enhancing the magnitude and durability of the $CD4^+$ T cell recall response following a second infection. Targeting IFN-driven Tr1 cell activity therefore represents a promising host-directed strategy to improve malaria immunity.

150 word:

Type I interferon (IFN) signalling promotes type 1 regulatory (Tr1) $CD4^+$ T cells, which suppress inflammation but may also limit protective Th1 and T follicular helper (Tfh) cell responses in malaria. We tested whether transient blockade of IFN-driven JAK/STAT signalling with ruxolitinib would reduce Tr1 cell activity and enhance protective $CD4^+$ T cell responses. In controlled human malaria infection, we assessed the impact of ruxolitinib on $CD4^+$ T cell activation and antigen-specific responses. Ruxolitinib suppressed pSTAT1, pSTAT3, and pSTAT5 in $CD4^+$ T cells during treatment but preserved antigen-specific responses. Notably, ruxolitinib treatment in first infection enhanced recall $CD4^+$ T cell responses during second infection, with increased frequencies of antigen-specific Th1, Tfh, and Tr1 cell subsets. These findings indicate that transient JAK inhibition reshapes the balance of Th1, Tfh and Tr1 cell subsets, and enhances the magnitude and durability of the $CD4^+$ T cell recall response following a second infection.

Summary: Blocking type I IFN signalling with ruxolitinib transiently reduces Tr1 cell activity while enhancing Th1 and Tfh cell recall responses, reshaping anti-parasitic $CD4^+$ T cell-mediated immune responses in malaria.

Introduction

Malaria remains a major global health threat, with 282 million cases and 610,000 deaths reported by the World Health Organisation in 2024. In addition to this health burden, malaria imposes significant socioeconomic costs on endemic communities (WHO, 2025). The recent approval of the pre-erythrocytic vaccines RTS,S and R21 marks a significant milestone in the development of tools to control malaria. However, protection is limited to young children, wanes over time, and falls short of the World Health Organisation's 75% efficacy target (Olotu et al., 2016). Suboptimal vaccine performance has been linked to baseline immune characteristics (Moncunill et al., 2022; Oyong et al., 2023), which not only shape responses to re-infection and vaccination, but may also influence the efficacy of anti-parasitic drugs (Rogerson et al., 2010). A deeper understanding of these immune networks may lead to the development of approaches to modulate immunity and therefore improve vaccine efficacy (Boyle et al., 2024; Montes de Oca et al., 2016a; Nahrendorf et al., 2021).

$CD4^+$ T cells are central to malaria immunity, coordinating responses against infection and regulating inflammation (Sallusto, 2016). IFNγ-producing Th1 cells promote antigen presentation by dendritic cells and activate macrophages to eliminate infected red blood cells (Tubo and Jenkins, 2014). There is significant heterogeneity in the molecules expressed by Th1 cells, in part due to tissue-specific adaptions in response to infection-mediated changes to inflammation and metabolism (Tuzlak et al., 2021). However, the inflammatory activity of Th1 cells must be counterbalanced to avoid immunopathology. In malaria, type 1 regulatory (Tr1) cells are important for this process via the secretion of IL-10 and expression of other inhibitory mediators, including co-inhibitory receptors (Boyle et al., 2015a; Boyle et al., 2017; Jagannathan et al., 2014; Montes de Oca et al., 2016c; Walther et al., 2009). While Tr1 cells limit immunopathology and thus disease (Edwards et al., 2023; Roncarolo et al., 2014; Roncarolo et al., 2018), they can also suppress Th1 and T-follicular helper (Tfh) cell development and function, potentially undermining protective immunity, vaccine efficacy, and memory (Montes de Oca et al., 2016b; Montes de Oca et al., 2016c; Zander et al., 2016). Tfh cells are essential for parasite-specific antibody responses. They support germinal centre B cell expansion and differentiation, thus driving the production of protective antibodies (Obeng-Adjei et al., 2015; Ryg-Cornejo et al., 2016). Functionally distinct Tfh subsets emerge during infection, and evidence from controlled human malaria infection (CHMI), field studies, and vaccine trials shows that Tfh2 and some Tfh1 cell subsets are particularly important for generating effective antibody responses (Bentebibel et al., 2013; Chan et al.,

2022; Chan et al., 2020; Morita et al., 2011; Nielsen et al., 2021; Soon et al., 2025). Thus, the balance between Th1, Tfh, and Tr1 cell subsets is central to shaping the quality of anti-parasitic immunity in malaria.

Recent work highlights type I interferons (IFNs) as key regulators of $CD4^+$ T cell subset balance. In experimental malaria models, type I IFNs suppress Th1 and Tfh cell differentiation while promoting Tr1 cell development (Nahrendorf et al., 2021; Zander et al., 2016). In CHMI studies, type I IFNs limited antigen-specific IFNγ production while enhancing parasite-specific IL-10 (Montes de Oca et al., 2016c). Additionally, STING-driven type I IFN signalling in $CD4^+$ T cells directly promotes Tr1 cell differentiation in humans (Wang et al., 2023). Targeting this pathway with the JAK1/2 inhibitor ruxolitinib, co-administered with anti-parasitic treatment, boosted anti-parasitic Th1 cell responses in a pre-clinical model of visceral leishmaniasis (VL), and *ex vivo* in blood samples from VL patients (Kumar et al., 2020). We recently reported that ruxolitinib when co-administered with standard antimalarial treatment was well tolerated in healthy volunteers experimentally infected with blood-stage *Plasmodium falciparum,* attenuated the post-treatment inflammatory response, and remodelled the systemic immune response to a second infection (Chughlay et al., 2022; Webster et al., 2025). Here, in this same study cohort, we investigate the impact of ruxolitinib as a host-directed treatment on $CD4^+$ T cell responses during malaria. We assess how transient blockade of type I IFN signalling can modulate the Th1, Tfh and Tr1 cell development and expansion with the goal of improving protective, anti-parasitic immunity.

Results

Ruxolitinib transiently inhibits JAK/STAT signalling in $CD4^+$ T cells during malaria

To investigate the impact of ruxolitinib host-directed therapy on the immune response during malaria, we used samples collected from a Phase 1b clinical trial (ACTRN12621000866808) (Webster et al., 2025). In this study, 20 malaria-naïve volunteers were infected with *P. falciparum*-parasitised red blood cells (pRBCs). On day 8 or 9 post-infection, participants were randomised to receive standard anti-malarial treatment (artemether-lumefantrine) with either ruxolitinib (20mg) or placebo, all administered twice daily for three days. Fifteen participants were re-inoculated three months later (Fig. 1A) and the resultant infection treated with artemether-lumefantrine. Trial safety, impact on clinical parameters and plasma cytokine responses have recently been reported (Webster et al., 2025). To examine the impact of

130 ruxolitinib on $CD4^+$ T cell signalling, whole blood was stimulated with IFNβ, IL-2,
131 PMA/ionomycin, or left unstimulated. Phosphoproteins were analysed at inoculation (I),
132 treatment day (T), 1.5 days after treatment (T+1.5; after three doses of ruxolitinib or placebo),
133 and five days after treatment commenced (T+5). Sampling strategy, immune cell subset
134 identification, and responses to IL-6 stimulation were previously described (Webster et al.,
135 2025).

136 Type I interferon signalling is critically dependent on the phosphorylation of STAT
137 transcription factors, which enables their dimerization, nuclear translocation, and induction of
138 interferon-stimulated genes (Platanias, 2005). Prior to inoculation, IFNβ stimulation
139 increased pSTAT1 and pSTAT3, while both IFNβ and IL-2 increased pSTAT5 in $CD4^+$ T
140 cells (Fig. 1B). PMA/ionomycin induced pCREB, pERK, and pS6 (Supplementary Fig. 1A).
141 Based on these findings, in subsequent analyses we focused on all signalling molecules in
142 unstimulated cells (to assess *in vivo* responses) and on molecules upregulated by stimulation
143 (pSTAT1, 3 and 5 for IFNβ, pSTAT5 for IL-2, and pERK/pCREB/pS6 for PMA/ionomycin).
144 $CD4^+$ T cell subsets were defined by CD127, CD27, CD38, HLA-DR, CD25, and CD45RA
145 to identify naïve, regulatory T (Treg), central memory (CM), effector memory (EM) and
146 activated (Act) cells (Fig. 1C). Phosphoprotein expression was analysed in $CD4^+$ T cells
147 using linear mixed-effects models, comparing I to T (infection response) and T to post-
148 treatment (treatment response, including ruxolitinib effects).

149 Infection upregulated pSTAT1 and pSTAT3 across all $CD4^+$ T cell subsets, revealing the
150 activation of these signalling pathways in $CD4^+$ T cells during infection (Fig. 1D,
151 Supplementary Fig. 1B). pSTAT5 only increased in Treg cells, indicating $CD4^+$ T cell subset-
152 specific activation (Supplementary Fig. 1B). Following treatment, placebo recipients showed
153 further increases in pSTAT1, pSTAT3, and pSTAT5 at T+1.5, consistent with responses to
154 dying parasites (Fig. 1D, Supplementary Fig. 1C). In contrast, ruxolitinib caused a marked,
155 but transient reduction in pSTATs at T+1.5 across all $CD4^+$ T cell subsets (Fig. 1D,
156 Supplementary Fig. 1D). By T+5, phosphoprotein levels returned to baseline in the placebo
157 group but remained elevated in the ruxolitinib group, suggesting prolonged $CD4^+$ T cell
158 activation (Fig. 1D).

159 Cytokine stimulation assays yielded similar effects, whereby ruxolitinib significantly reduced
160 IFNβ-induced pSTAT1, pSTAT3, and pSTAT5, as well as IL-2-induced pSTAT5, at T+1.5
161 (Fig. 1E, Supplementary Fig. 2A–D). Analysis of fold changes (T to T+1.5) revealed
162 consistent clustering by treatment group, where placebo participants showed increased

163 pSTAT expression, while ruxolitinib-treated participants showed reduced responses (Fig. 1F–
164 G). One participant who received only two ruxolitinib doses (participant D722, treatment
165 stopped due to as protocol-defined toxicity rules (Webster et al., 2025)) grouped with placebo
166 rather than ruxolitinib-treated participants. While pSTAT1 and pSTAT3 responses were
167 consistent across $CD4^+$ T cell subsets, pSTAT5 showed more variability amongst $CD4^+$ T
168 cell subsets in unstimulated conditions (Fig. 1F). Similar patterns of phosphorylation were
169 observed following IL-2 stimulation, although the effect was relatively uniform across all
170 $CD4^+$ T cell subsets (Supplementary Fig. 2C-E).

171 Beyond JAK/STAT activation, *P. falciparum* infection and treatment also affected other
172 $CD4^+$ T cell signalling pathways and pCREB, pERK, and pS6 levels declined following
173 treatment in unstimulated and in PMA/ionomycin stimulated responses (Supplementary Fig.
174 1E, Supplementary Fig. 3A). However, for pCREB this reduction was significantly greater in
175 placebo compared to ruxolitinib recipients (Supplementary Fig. 1F, Supplementary Fig. 3A).
176 Although more variable than changes in pSTATs (Supplementary Fig. 3B), these changes
177 indicate broader effects of *P. falciparum* infection on $CD4^+$ T cell signalling pathways, and
178 also suggest preservation of these pathways by ruxolitinib. Together, these findings
179 demonstrate that ruxolitinib effectively suppresses JAK/STAT signalling in $CD4^+$ T cells
180 during malaria, dampening both *in vivo* activation and IFNβ/IL-2-induced responses, while it
181 may preserve other mitogen-driven $CD4^+$ T cell signalling pathways, albeit in a more
182 heterogeneous way.

183

184

185

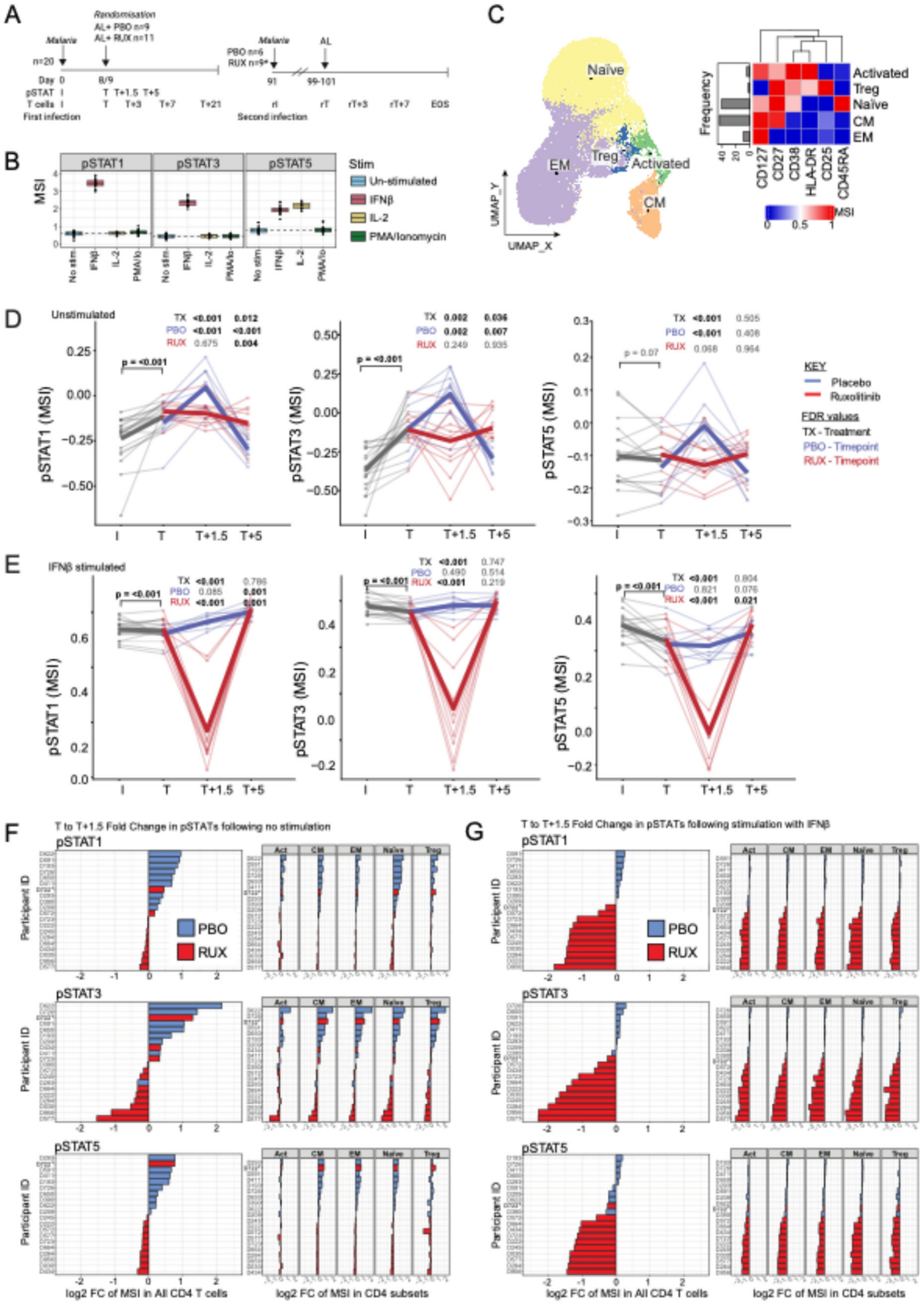

Figure 1. Ruxolitinib transiently reduces JAK/STAT signalling in CD4 T cells during malaria.

189 ***A)*** *Study design and whole blood sampling for pCyTOF of phosphoproteins (pSTAT), and T*
190 *cell analysis from peripheral blood mononuclear for CyTOF, flow cytometry, activation*
191 *induced marker (AIM) assays and single cell RNA and T cell receptor (TCR) sequencing*
192 *(scRNA/TCRseq). Inoculation (I), re-inoculation at days 90 post-infection (rI), treatment*
193 *during first (T) and second (rT) infection, as well as the end of study (EOS; ~28 days after*
194 *rT) are indicated. 20 participants were included in the first infection, and 15 in the second. ******
195 *One participant in the ruxolitinib group was treated early after inoculation due to COVID-19*
196 *infection.* ***B)*** *Phosphorylation of signalling molecules during malaria in unstimulated and*
197 *IFNβ, IL2 and PMA/ionomycin stimulated cells was analysed by pCyTOF at day of*
198 *inoculation, treatment (T), 1.5 days after treatment (T+1.5) and 5 days after treatment (T+5).*
199 *At inoculation, levels of phosphorylated (p)STAT1, pSTAT3 and pSTAT5 in CD4 T cells in*
200 *unstimulated and stimulated conditions are shown.* ***C)*** *CD4 T cells were characterised by*
201 *expression of CD127, CD27, CD38, HLA-DR, CD25 and CD45RA. Identified subsets and*
202 *expression of markers is shown.* ***D/E)*** *pSTAT1, pSTAT3, and pSTAT5 expression in*
203 *unstimulated* ***(D)*** *and IFNβ–stimulated* ***(E)*** *CD4 T cells at I, T, T+1, T+5. Data are log*
204 *transformed median signalling intensities, with thin lines representing each participant and*
205 *coloured by treatment group. All datapoints prior to randomisation are in grey; following*
206 *randomisation ruxolitinib-treated participants are shown in red and placebo treated*
207 *participants are in blue. P values are from linear mixed effect models, with bold lines*
208 *representing the mean of the predicted values from the fitted models for each group. TX*
209 *indicates the p values for the interaction term between each timepoint (compared to T) and*
210 *treatment groups. P values for comparisons between each timepoint and T are shown for the*
211 *placebo (PBO) and ruxolitinib (RUX) groups and were determined from contrasts.* ***F/G*** *Fold*
212 *change in expression of pSTAT1, pSTAT3, pSTAT5 between T and T+1.5 in total CD4 T cells*
213 *and CD4 T cell subsets for unstimulated (****F****) and IFNβ stimulated* ***(G)*** *cells. Data for each*
214 *participant are shown. See also Supplementary Figures 1-3.*

215

216 **Th1, Tfh and Tr1 cell responses are more rapidly activated in second infection and**
217 **modulated by ruxolinitib treatment**

218 To assess the impact of ruxolitinib on $CD4^+$ T cell subset development and expansion, we
219 performed high-dimensional surface phenotyping CyTOF analysis of PBMCs at multiple
220 time points during the first and second infection (I, T, T+3, T+7, T+20; re-inoculation (rI),

221 rT, rT+3, rT+7, end of study (EOS)) (Supplementary Fig. 4A). $CD4^+$ T cells were identified
222 within PBMCs (Supplementary Fig. 4B-C), and then clustered based on chemokine receptors
223 and memory markers (CCR7, CXCR5, CXCR3, CCR6, CD45RA), regulatory markers
224 (CD127, CD25, LAG3, CD49b), and activation markers (CD38, PD1, ICOS, HLA-DR),
225 identifying 18 subsets (Fig. 2A-B).

226 Longitudinal analysis revealed distinct $CD4^+$ T cell dynamics in first and second infection,
227 which were modulated by ruxolitinib (Fig. 2C-D). During the first infection, there was a
228 reduced frequency of several $CD4^+$ T cell subsets, including activated Th1 and Tr1 cells
229 between inoculation and treatment (Fig. 2E-F, Supplementary Fig. 4D). This is consistent
230 with other human studies that show transient reductions of circulating $CD4^+$ T cell subsets
231 during acute malaria, with recovery after treatment and accompanying evidence that
232 lymphocytes relocate to secondary lymphoid tissues (Boyle et al., 2015b; Mandala et al.,
233 2022; van Wolfswinkel et al., 2017). After treatment, activated Th1 cell frequency increased
234 at both T+3 and T+7, consistent with strong $CD4^+$ T cell activation (Fig. 2C). Activated Tfh2
235 cells decreased, and Tr1 cell frequencies remained low. Ruxolitinib modestly affected the
236 frequencies of Tr1 and activated Tfh2 cells, but overall changes were small (Fig. 2C). In the
237 second infection, multiple $CD4^+$ T cell subsets, including activated Th1 and Tfh cell
238 populations, expanded more rapidly, with the greatest changes at rT+3, consistent with a
239 recall response. Unlike in the first infection, ruxolitinib significantly modulated these recall
240 responses, including increased frequencies of Th1 cells and activated Tfh1 and Tfh2 cells
241 (Fig. 2D). $CD4^+$ T cell subset-specific kinetics were also evident (Fig. 2E-F, Supplementary
242 Fig. 4D-E). For example, activated Th1 cells peaked at T+7 in the first infection but at rT+3
243 in the second, and were not affected by ruxolitinib. Similar trends were observed for
244 $CD38^+ICOS^+$ Th1 cells (Supplementary Fig. 4D-E). $CD38^+$ Tfh1 cells showed minimal
245 change in the first infection but expanded at all post-treatment time points in the second
246 infection, with markedly higher frequencies in ruxolitinib-treated participants at EOS. Similar
247 kinetics were observed for $CD38^+$ $PD1^+$ $ICOS^+$ Tfh1 and Tfh2 cells, which both also
248 remained significantly elevated in ruxolitinib recipients in second infection at EOS
249 (Supplementary Fig. 4D-E). Tr1 cells were detected at low frequency, possibly due to
250 staining limitations of LAG3 and CD49b in CyTOF, with a modest ruxolitinib-dependent
251 increase at T+7 during the first infection only (Fig. 2E-F). Together, these data indicate
252 comparable memory Th1 cell responses across treatment groups, but a more robust and

253 sustained germinal centre–associated response in ruxolitinib-treated participants during
254 second infection, reflected in sustained Tfh cell subset frequencies.

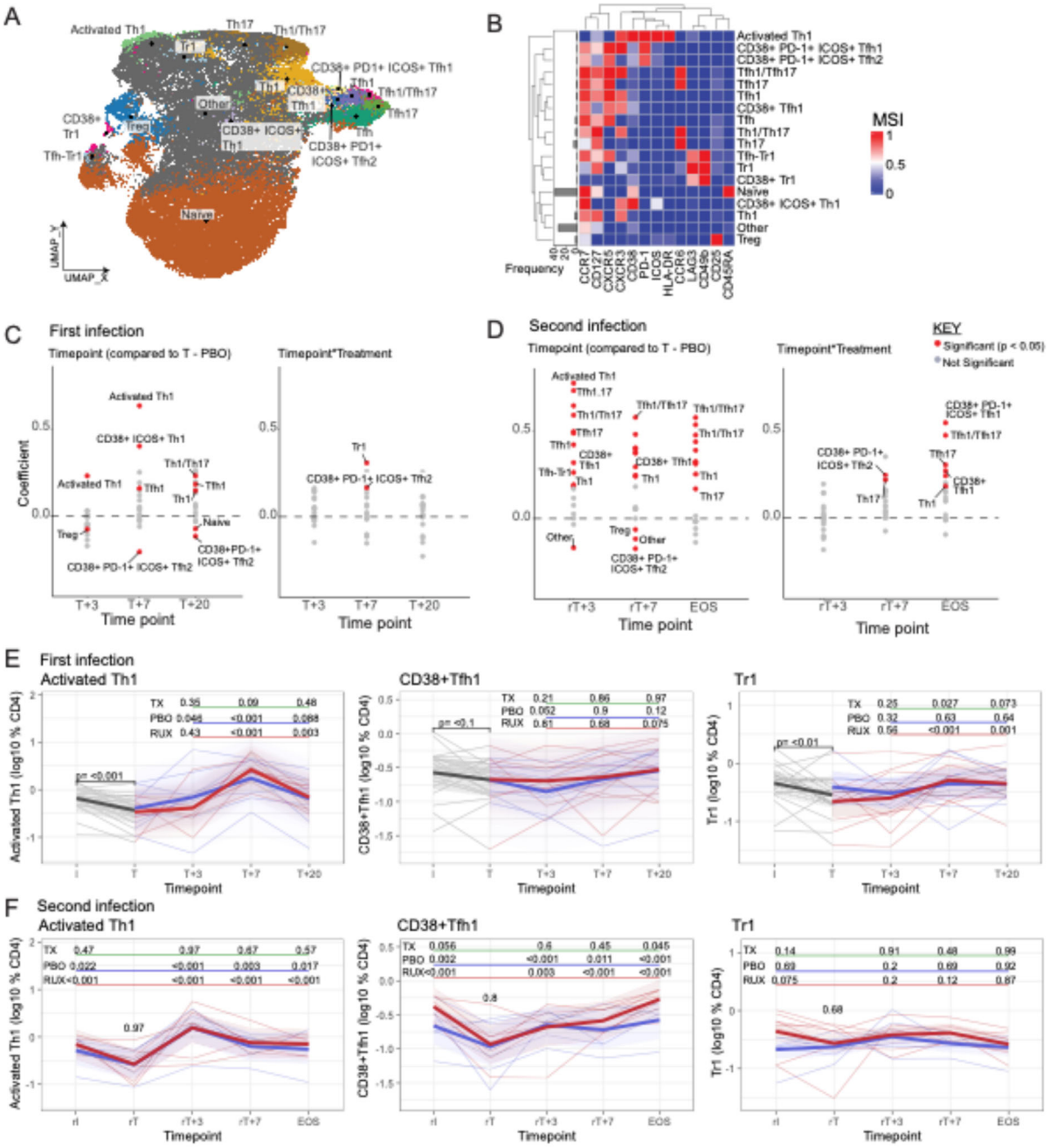

255

256 ***Figure 2: CD4 T cell subsets and activation in first and second infection.***

257 *CD4 T cells were analysed by CyTOF at inoculation (I), treatment (T) and post treatment*
258 *timepoints (T+3, T+7 and T+20) in first infection, and at re-inoculation (rI), re-treatment*
259 *(rT) and post treatment timepoints (rT+3, rT+7, EOS) in second infection.* ***A)*** *UMAP and* ***B)***
260 *cluster marker expression of identified CD4 T cell subsets.* ***C/D)*** *Coefficient from mixed effect*
261 *models analysing CD4 T cell subsets, analysing changes with time compared to treatment (T*

262 *in first infection and rT in second infection), and the interaction between time and ruxolitnib*
263 *treatment (Timepoint*Treatment). Significant changes are indicated in red. Coefficient of*
264 *zero, indicating no change is marked by a dashed line.* ***E/F)*** *Activated Th1, CD38+ Tfh1 and*
265 *Tr1 cells in first and second infection. Data are log10 frequencies of CD4 T cells, with thin*
266 *lines representing each participant. All datapoints prior to randomisation are in grey;*
267 *following randomisation ruxolitinib-treated participants are in red and placebo-treated are*
268 *in blue. P values are from linear mixed effect models, with bold lines representing the mean*
269 *of the predicted values from the fitted models for each group. TX is p values for the*
270 *interaction term between each timepoint (compared to T) and treatment groups (underlined*
271 *with green). P values for the comparison between each timepoint and T are shown for the*
272 *placebo (PBO, underlined with blue) and ruxolitinib (RUX, underlined with red) groups, and*
273 *were determined from contrasts. P value for the difference at rT between placebo and*
274 *ruxolitinib group, calculated from the intercept is shown at rT. See also Supplementary*
275 *Figure 4.*

276

277 **Ruxolitinib transiently delays induction of co-inhibitory rich Tr1 cell subsets during**
278 **first infection**

279 We and others have previously reported on the phenotypic heterogeneity of Tr1 cells and the
280 impact this has on regulatory function (Brockmann et al., 2018; Edwards et al., 2023). We
281 developed an optimised spectral flow cytometry panel to identify Tr1 cells and to characterise
282 their phenotype in detail (Supplementary Fig. 5). To assess whether ruxolitinib influenced
283 Tr1 cell phenotype and functional potential, we examined co-inhibitory receptors (CIR:
284 CTLA4, CCR2, TIM3, CCR5, TIGIT, PD1), memory markers (CD45RA, CCR7, CXCR5,
285 CXCR3, CD161), and activation/proliferation markers (Ki67, CD38, ICOS) using unbiased
286 clustering (Fig. 3A-B). Ten Tr1 clusters were identified. Four clusters (C4, C5, C6, C10)
287 were CIR-rich, expressing high levels of 4–5 CIRs, and overlapped with Tfh ($CXCR5^+$) and
288 Th1 ($CXCR3^+$) cell phenotypes, consistent with PBMC data (Fig. 2). Cluster C4 also had
289 elevated expression of Ki67, ICOS, and CD38 expression, indicating an activated and
290 proliferating status (Fig. 3B).

291 During first infection, multiple Tr1 clusters expanded, including CIR-rich and activated C4
292 and C6 clusters at T+3 and T+7, alongside expansion of an activated cluster (C8). In contrast,
293 naïve-like clusters (C1, C5; $CD45RA^+$) or non-activated clusters (C10) contracted.

294 Importantly, the expansion of the most CIR-rich and activated cluster, C4, was significantly
295 reduced in ruxolitinib-treated participants at T+3, and this effect was transient, with
296 frequencies equalising by T+7 (Fig. 3C-D). In contrast, naïve, and non-activated clusters (C1,
297 C2 and C5) were relatively expanded in ruxolitinib-treated participants at T+3 (Fig. 3C). In
298 second infection, the highly activated CIR-rich C4 cluster (C4) re-expanded, peaking at rT+3,
299 and expansion was not influenced by ruxolitinib treatment in first infection (Fig. 3E-F).
300 Together, these results show that ruxolitinib transiently suppresses the induction of Tr1 cell
301 subsets with high activation and inhibitory potential during first infection but does not show a
302 long-term effect on the capacity of Tr1 cells to expand during a second infection.

303

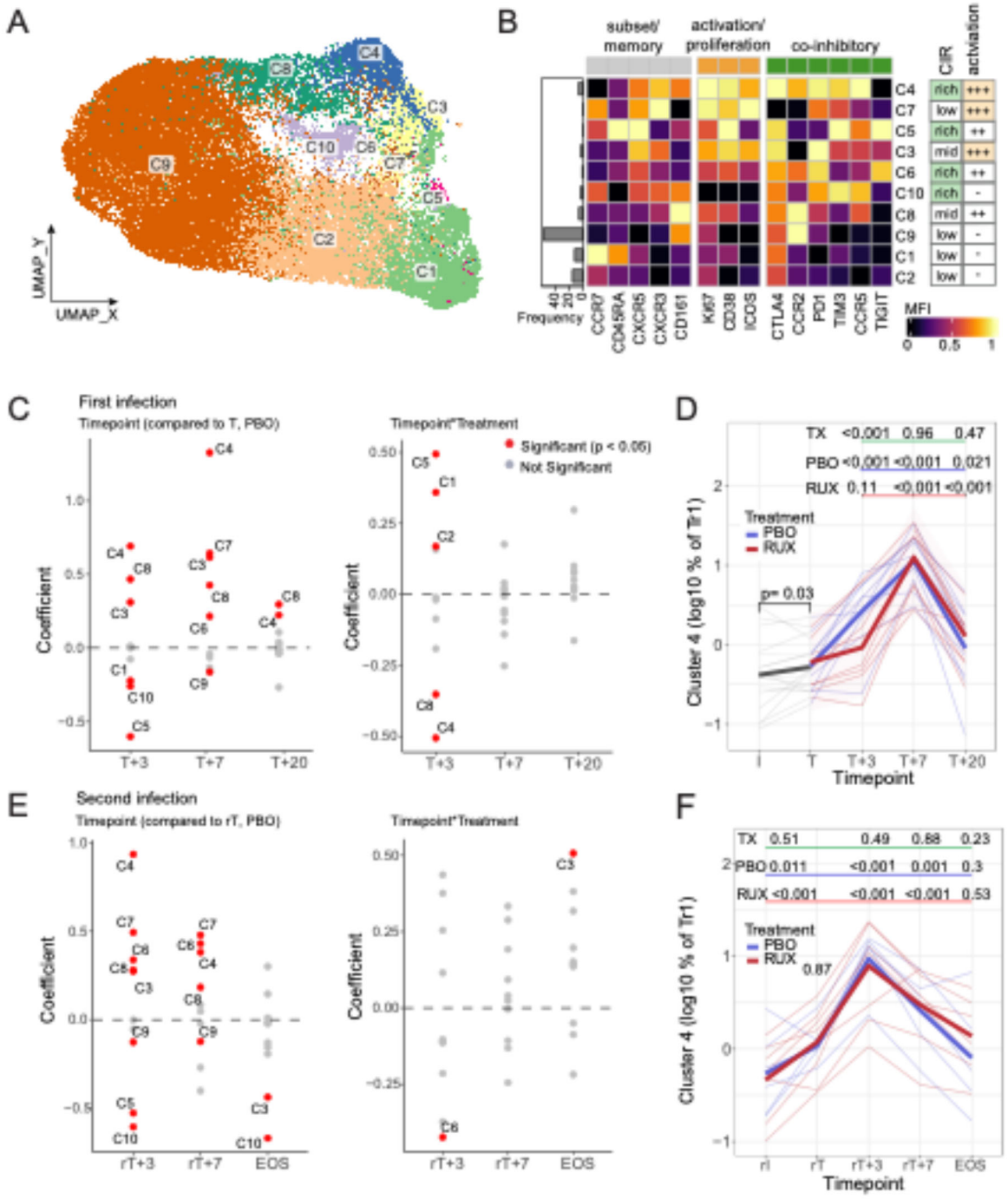

Figure 3: Induction of Tr1 co-inhibitory receptor rich CD4 T cells and impact of ruxolitinib.

A/B) *UMAP of Tr1 CD4 T cell clusters based on expression of subset, memory, activation, proliferation and co-inhibitory receptor (CIR) markers showed in heatmap.* ***C)*** *Expression of markers on subsets identified within Tr1 cells. CIR rich subsets are indicated. Subsets identified were analysed in mixed models in first and second infection as a proportion of total*

Tr1 cells. ***D/F)*** *Coefficient from mixed effect models analysing Tr1 cell subsets, analysing changes with time compared to treatment (T in first infection and rT in second infection), and the interaction between time and ruxolitnib treatment (Timepoint*Treatment). Significant changes are indicated in red. Coefficient of zero, indicating no change, is marked by a dashed line.* ***A/E/G)*** *Data are log10 frequencies of CD4 T cells, with thin lines representing each participant. Prior to randomisation data are in grey; following randomisation ruxolitinib-treated participants are red and placebo-treated participants are blue. P values are from linear mixed effect models, with bold lines representing the mean of the predicted values from the fitted models for each group. TX is p values for the interaction term between each timepoint (compared to T) and treatment groups. p values for the comparison between each timepoint and T are shown for the placebo (PBO) and ruxolitinib (RUX) groups, which were determined from contrasts. P value for the difference at rT between placebo and ruxolitinib group, calculated from the intercept is shown at rT. See also Supplementary Figure 5.*

Effects of ruxolitinib on antigen-specific CD4$^+$ T cell responses during first and second infection

To examine malaria-specific CD4$^+$ T cell responses, we performed Activation-Induced Marker (AIM) assays with pRBC stimulation on samples collected during first and second infection (I, T, T+3, T+7, T+20; rI, rT, rT+3, rT+7, EOS). Malaria-specific CD4$^+$ T cells were identified by OX40 and CD69 expression (AIM$^+$ cells), and subsets defined using CXCR5, PD1, CXCR3, CCR6, LAG3, CD49b, and CCR4 (Fig. 4A, Supplementary Fig. 6). Identified subsets included Tr1 (LAG3$^+$ CD49b$^+$), Tfh (CXCR5$^+$ PD1$^+$, LAG3$^-$ CD49b$^-$), Th1 (CXCR3$^+$ CCR4$^-$ CCR6$^-$), Th2 (CXCR3$^-$ CCR4$^+$ CCR6$^-$), and Th17 (CXCR3$^-$ CCR4$^-$ CCR6$^+$) cells. Within Tr1 cells, Tfh.Tr1 cells (CXCR5$^+$ PD1$^+$) were also analysed, and Tfh cell subsets were further classified (Tfh1, Tfh2, Tfh17), as for Th1, Th2 and Th17 cell lineages.

In the first infection, AIM$^+$ CD4$^+$ T cells increased significantly at T+7 and T+20 across all subsets (Fig. 4B). Induction of AIM$^+$ CD4$^+$ T cells was comparable between placebo- and ruxolitinib-treated participants, consistent with findings in the total CD4$^+$ T cell compartment (Fig. 2). By the time of second infection (rI), AIM$^+$ CD4$^+$ T cell frequencies had returned to baseline, except for AIM$^+$ Tfh1 cells, which remained elevated (Supplementary Fig. 7A).

343 Following the second infection, $CD4^+$ T cell AIM^+ responses re-emerged but were restricted
344 to Th1, Tfh, and Tr1 (notably Tfh.Tr1) cell subsets, indicating a more focused recall response
345 (Fig. 4C). In contrast to the first infection, ruxolitinib-treated participants showed a
346 significantly stronger and faster recall response, particularly within the Tfh cell compartment,
347 and these responses remained elevated compared to placebo at EOS (Fig. 4C).

348 Analysis of $CD4^+$ T cell subset frequencies over time revealed that in the first infection,
349 AIM^+ Th1, Tfh, and Tr1 cell frequencies peaked at T+7 and remained elevated at T+20 (Fig.
350 4D), while AIM^+ Th2 and Tfh2 peaked later at T+20 (Supplementary Fig. 7B). During the
351 second infection, an earlier and more sustained antigen-specific responses were observed in
352 ruxolitinib-treated participants. The frequencies of total AIM^+ $CD4^+$ T cells, as well as AIM^+
353 Th1, Tfh1, Tr1 and total Tfh cells were significantly higher in the ruxolitinib group at rT+3
354 and EOS, compared with placebo (Fig. 4C & E, Supplementary Fig. 7C). Together, analyses
355 of both the total and antigen-specific $CD4^+$ T cell compartments indicate that while
356 ruxolitinib had limited observable effect on responses during the first malaria infection, its
357 administration at first infection enhanced the magnitude and duration of the $CD4^+$ T cell
358 recall response following a second infection, most notably within the Tfh cell lineage.

359

360

361

362

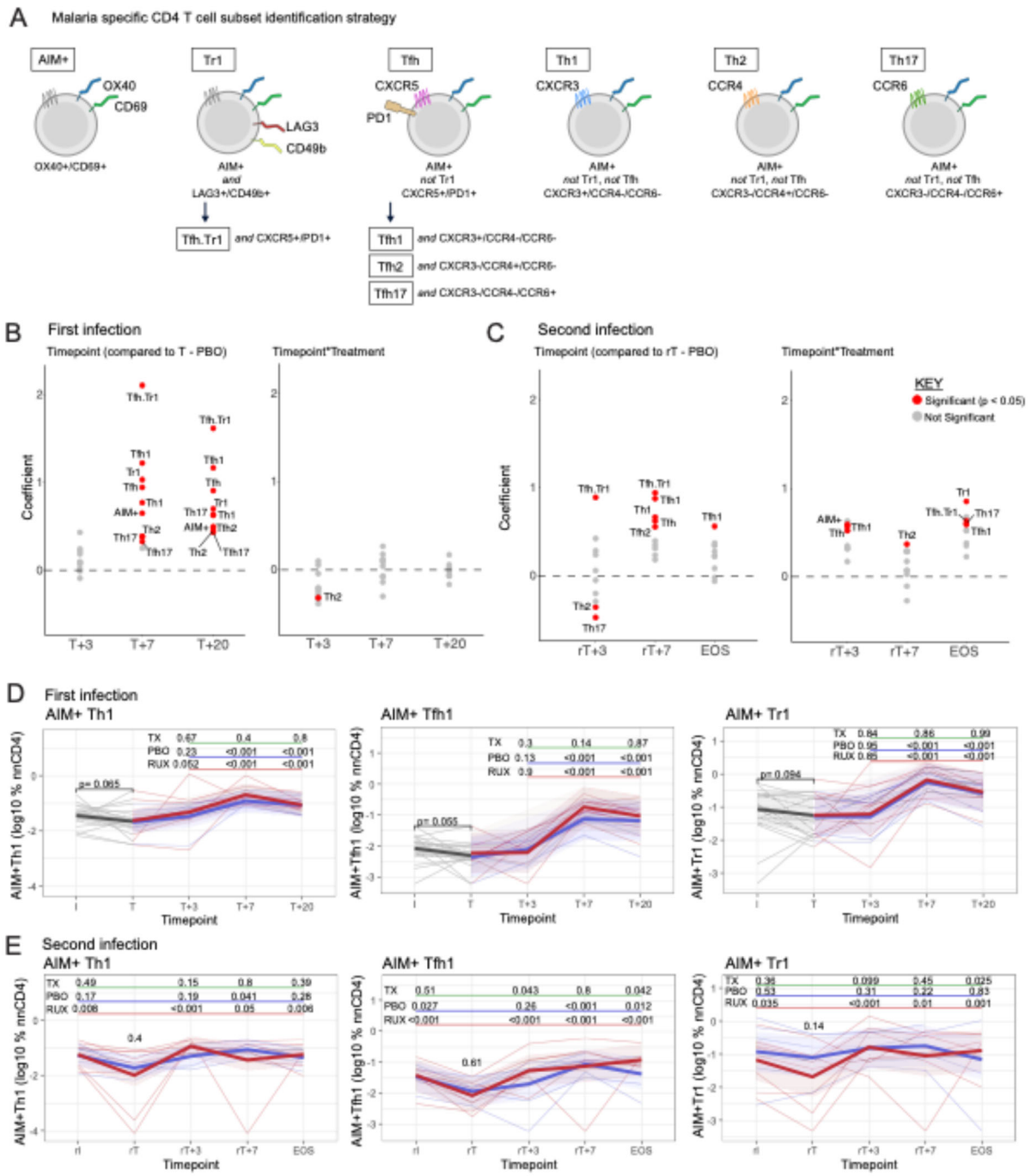

363

364 ***Figure 4: Malaria specific CD4 T cell responses during first and second infection.***

365 *Parasite specific CD4 T cells were identified using Activation Induced Marker assay at*
366 *inoculation (I), treatment (T) and post treatment timepoints (T+3, T+7 and T+20) in first*
367 *infection, and at re-inoculation (rI), re-treatment (rT) and post treatment timepoints (rT+3,*
368 *rT+7, EOS) in second infection.* ***A)*** *Schematic of identified CD4 T cell subsets.* ***B/C)***
369 *Coefficient from mixed effect models analysing CD4 T cell subsets, analysing changes with*
370 *time compared to treatment (T in first infection and rT in second infection), and the*
371 *interaction between time and ruxolitnib treatment (Timepoint*Treatment). Significant*

372 *changes are indicated in red. Coefficient of zero, indicating no change is marked by a dashed*
373 *line.* ***D/E)*** *AIM+ Th1, AIM+ Tfh1 and AIM+ Tr1 cells in first and second infection. Data are*
374 *log10 frequencies of malaria specific AIM+ CD4 T cells, with thin lines representing each*
375 *participant. Prior to randomisation is in grey, following randomisation ruxolitinib-treated*
376 *participants are red and placebo-treated are blue. P values are from linear mixed effect*
377 *models, with bold lines representing the mean of the predicted values from the fitted models*
378 *for each group. TX is p values for the interaction term between each timepoint (compared to*
379 *T) and treatment groups (underlined in green). P values for the comparison between each*
380 *timepoint and T are shown for the placebo (PBO, underlined in blue) and ruxolitinib (RUX,*
381 *underlined in red) groups, which were determined from contrasts. P value for the difference*
382 *at rT between placebo and ruxolitinib group, calculated from the intercept is shown at rT.*
383 *See also Supplementary Figure 6 & 7.*

384

385 **Th1, Tfh and Tr1 cells share overlapping transcriptional profiles and emerge rapidly**
386 **after anti-parasitic drug treatment following second infection**

387 To better understand the impact of ruxolitinib on primary and recall $CD4^+$ T cell responses,
388 we used scRNA/TCRseq to transcriptionally profile responses in 8 participants during first
389 and second infection (n=4 placebo, n=4 ruxolitinib, 10 timepoints each) (Fig. 5A). Antigen
390 experienced $CD4^+$ T cells ($CD45RA^-$) were sorted by flow cytometry and analysed, and
391 malaria-specific cells were also identified by AIM assays, sorting $CD69^+/OX40^+$ cells for
392 sequencing (Fig. 5A, Supplementary Fig. 8A-B). scRNAseq data from antigen-experienced
393 $CD4^+$ T cells and AIM^+ $CD4^+$ T cells were integrated based on donor (Fig. 5B). The
394 unstimulated antigen-experienced $CD4^+$ T cells were then selected for downstream clustering
395 and annotation. Ten $CD4^+$ T cell clusters were identified from 127,482 high quality
396 unstimulated cells (Fig. 5C, Supplementary Fig. 8C-E).

397 $CD4^+$ T cell clusters included Th1, Tfh and Tr1 cell subsets. Th1 cells were identified based
398 on elevated *CXCR3, CCL5, TBX21* (encoding T-bet), and cytotoxic markers *NKG7, GNLY,*
399 *GZMB* and *PRF1;* Tfh cells could be identified based on elevated *CXCR5*, *TOX2*, *ICOS*, and
400 *BCL6*; and Tr1 cells could be identified based on elevated *IL10*, *CCR5*, *LAG3*, *HAVCR2*
401 (encoding Tim3), and *PRDM1* (encoding BLIMP1) (Fig. 5D). Consistent with the
402 overlapping phenotypes of Tr1 cells with Th1 and Tfh cells (Fig. 2, 3 & 4), the Tr1 cell
403 cluster also expressed high levels of Th1 cell markers including *IFNG, CXCR3, TBX21* and

404 Tfh cell markers including *CXCR5* and *BCL6* (Fig. 5D). A cycling cell cluster was also
405 identified based on expression of *MKI67 (*encoding Ki67), which also expressed high levels
406 of *CD38* consistent with activation. This cycling cluster shared gene expression profiles with
407 Th1 (including *IFNG* and *CXCR3)*, Tfh (including *TOX2* and *IL21*) and Tr1 (including *LAG3*
408 and *HAVCR2)* cells (Fig. 5D). The shared gene expression by Th1, Tfh and Tr1 cells was also
409 confirmed by analysis of all cluster marker genes, which identified 1098 overlapping marker
410 genes between Tfh and Tr1 cells, 186 genes between Th1 and Tr1 cells and 270 genes
411 between cycling, Tfh and Tr1 cells (Fig. 5E).

412 In addition to the Th1, Tfh, and Tr1 cell clusters, several other $CD4^+$ T cell subsets were
413 identified. Th17 cells were defined by expression of *CCR6* and *RORC*; central memory T
414 (Tcm) cells by expression of *CCR7*; regulatory T (Treg) cells by expression of *FOXP3* and
415 *IL2RA*; and Th2 cells by expression of *GATA3*. Two smaller clusters were also detected: one
416 characterised by high expression of type I interferon–stimulated genes (ISGs), including
417 *IFIT2*, *IFIT1*, and *IFIT3*; and another marked by elevated heat shock protein expression (HSP
418 stress cluster) (Fig. 5C-D). The distribution of these $CD4^+$ T cell clusters varied by donor,
419 treatment group and timepoint (Supplementary Fig. 8F-H).

420 Further sub-clustering of Th1, Tfh and Tr1 cells revealed substantial heterogeneity within
421 each subset. Tr1 cells segregated into three distinct transcriptional clusters: a co-inhibitory
422 receptor–rich cluster characterised by elevated *CCR2*, *CCR5*, *LAG3*, and *HAVCR2* (encoding
423 TIM-3) expression; a memory-like cluster defined by *CXCR5* and *CCR7* expression; and a
424 proliferating cluster marked by *MKI67* expression (Supplementary Fig. 9A-B). The
425 proportions of these Tr1 cell sub-clusters varied across timepoints, with the CIR-rich cluster
426 relatively reduced at T+7 in first infection in ruxolitinib-treated participants and with all three
427 appearing more frequent in ruxolitinib-treated participants during the second infection at the
428 rT+3 timepoint (Supplementary Fig. 9C). Tfh cells were further divided into six clusters: a
429 Tfh/Th17 cell-like cluster, a Tfh cell effector cluster, a Tfh cell activated cluster, a Tfh cell
430 $AREG^+$ cluster, a Tfh cell stress cluster, and a Tfh cell $ID3^+$ cluster (Supplementary Fig. 9D-
431 E). The frequencies of these clusters also varied with timepoint and treatment. Notably, the
432 Tfh activated cell cluster, with elevated expression of *CD38* and *HLA-DRA*, was increased in
433 ruxolitinib-treated participants following second infection at the late timepoint of rT+20,
434 consistent with enhanced activation or persistence of Tfh cell responses (Supplementary Fig.
435 9F). Th1 cells could be divided into six clusters, including three cytotoxic clusters
436 distinguished by expression of *GNLY*, *GZMB*, *CCL4*, and *CCL3*; two Th1/Th17 cell-like

437 clusters expressing *CCR6* and *CXCR3*; and a Th1/Tfh/Tr1 cell-like cluster expressing *IL10*,
438 *CXCR5* and *CXCR3* (Supplementary Fig. 9G-H). The distribution of Th1 cell sub-clusters
439 also differed across timepoints and between treatment groups (Supplementary Fig. 9I).

440 While frequencies of $CD4^+$ T cell clusters differed across participants (Fig. 5F), there was a
441 clear expansion of Th1, Tfh and Tr1 cells in response to malaria. Following first infection,
442 Tr1, Tfh and cycling cells expanded at T+7; these appeared higher in ruxolitinib-treated
443 participants for cycling cells (Fig. 5G; Supplementary Fig. 9I). In second infection, the re-
444 emergence of cycling, and Tr1, Tfh, Th1 cell subsets occurred earlier in infection at rT+3,
445 consistent with CyTOF and flow cytometry data (Fig. 2 & 3). A robust recall response was
446 also measured during second infection, particularly in cycling cells from ruxolitinib-treated
447 participants (Fig. 5H, Supplementary Fig. 9J). Thus, these results support earlier findings
448 from CyTOF and flow cytometry analysis and reinforce the impact of ruxolitinib treatment
449 during first infection on modulating the expansion and balance of Th1, Tr1 and Tfh cells
450 during second infection. Furthermore, transcriptional overlap between Th1, Tr1 and Tfh cells
451 was observed, suggesting plasticity in these $CD4^+$ T cell subsets.

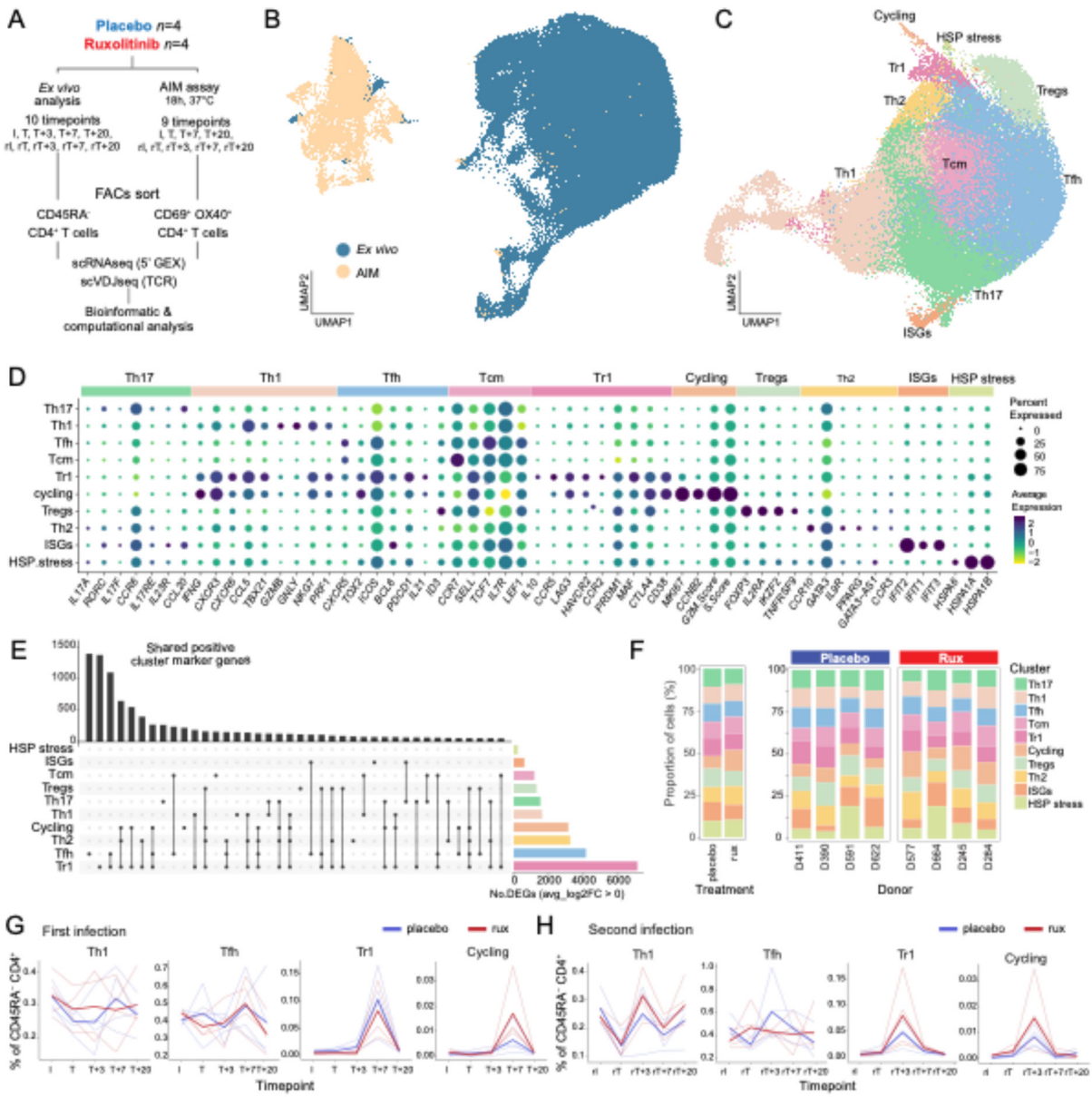

Figure 5: scRNAseq reveals overlapping Th1, Tfh and Tr1 transcriptional profiles.

A) *Experimental design showing scRNA/TCRseq profiling of antigen experienced (CD45RA⁻) CD4⁺ T cells (Ex vivo) and malaria specific (CD69⁺OX40⁺) CD4⁺ T cells identified by AIM assays (AIM) from 8 participants (n = 4 placebo, n = 4 ruxolitinib) across 9 – 10 timepoints during first and second infection.* ***B)*** *UMAP visualisation showing the Ex vivo and AIM cells after integration by donor.* ***C)*** *UMAP visualisation showing Ex vivo cells after subsetting and performing unsupervised clustering analysis.* ***D)*** *Dot plot showing the average expression of curated marker genes for each Ex vivo cluster.* ***E)*** *Upset plot showing the number of shared marker genes between Ex vivo clusters. The bar graph on the right shows the total number of differentially expressed cluster marker genes for each subset.* ***F)*** *Stacked bar plots showing the proportion of cells within each cluster by treatment and donor.* ***G)*** *Line graphs showing*

464 *the cluster frequency as a percentage of total Ex vivo CD4$^+$ T cells during the first and* ***H)***
465 *second infections. Lines are coloured by treatment group, with bold lines representing group*
466 *means and transparent lines showing individual donor values. See also Supplementary*
467 *Figures 8 & 9.*

468

469 **Ruxolitinib treatment promotes a pro-inflammatory gene signature in CD4$^+$ T cells**

470 We next examined the hallmark IFN-alpha response gene signature across CD4$^+$ T cell
471 subsets between ruxolitinib- and placebo-treated participants. Across all subsets, ruxolitinib
472 treatment was associated with significantly reduced IFN-alpha response scores at T+3,
473 consistent with suppression of type I IFN–driven pathways by ruxolitinib treatment (Fig. 6A).
474 To determine the impact of ruxolitinib on the transcriptional landscape of Th1, Tfh, and Tr1
475 cells, we performed pseudobulk differential gene expression analysis between ruxolitinib-
476 and placebo-treated cells (Fig. 6B). This analysis was performed at T+7 during first infection
477 and rT+3 following the second infection, as these timepoints represented peak CD4$^+$ T cells
478 responses (Fig. 2-5). We identified 275 differentially expressed genes (DEGs) at T+7 (147
479 upregulated in ruxolitinib, 128 in placebo) and 262 DEGs at rT+3 (143 up in ruxolitinib, 119
480 in placebo) in Tr1 cells. Genes upregulated in ruxolitinib-treated Tr1 cells included cytotoxic
481 genes such as *GZMA*, *GZMH*, *NKG7*, and *GNLY*, suggesting relatively enhanced cytotoxic
482 potential (Fig. 6B). Pathway analysis indicated enrichment of the Interferon Gamma
483 Response pathways in ruxolitinib-treated participants during first and second infection, along
484 with other inflammatory pathways (Fig. 6C). Tfh cell analysis revealed 434 DEGs at T+7
485 (234 up in ruxolitinib, 200 in placebo) and 338 DEGs at rT+3 (194 up in ruxolitinib, 144 in
486 placebo) (Fig 6B). Again, pathway analysis highlighted Hallmark Interferon Gamma
487 Response pathways enrichment in Tfh cells from ruxolitinib-treated donors during first and
488 second infection (Fig 6C). We also identified 182 DEGs at T+7 (118 up in ruxolitinib, 64 in
489 placebo) and 178 DEGs at rT+3 (105 up in ruxolitinib, 73 in placebo) in Th1 cells (Fig. 6B),
490 and as expected for this CD4$^+$ T cell subset, Hallmark Interferon Gamma Response pathways
491 were enriched in ruxolitinib Th1 cells at both timepoints (Fig. 6C). Overall, these results
492 indicate that ruxolitinib drives antigen-specific CD4$^+$ T cell subsets towards a more pro-
493 inflammatory transcriptional signature that is maintained following re-exposure to parasite
494 antigen.

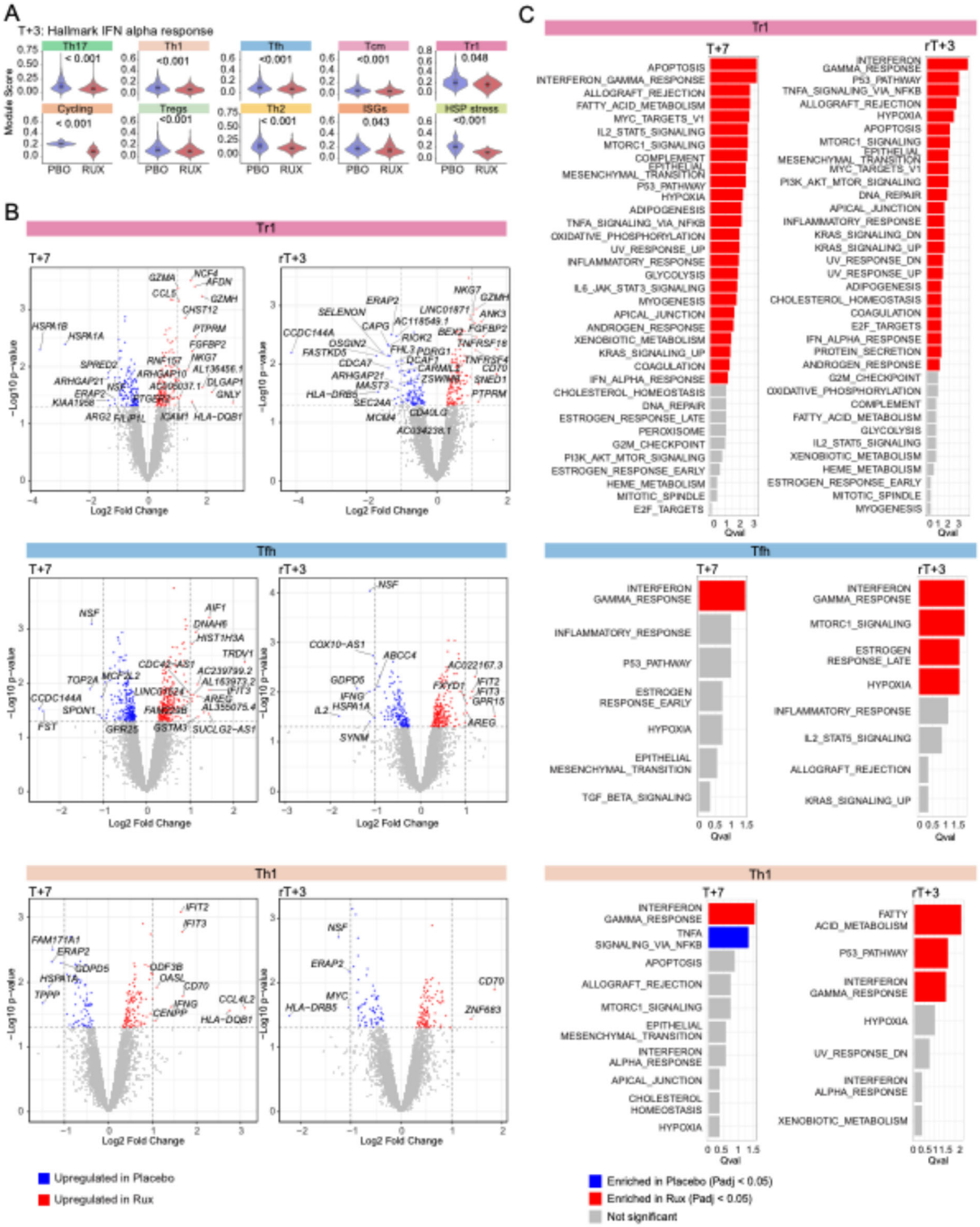

Figure 6: Ruxolitinib treatment promotes transcriptional programs associated with enhanced CD4⁺ T cell function.

A) *Violin plots showing the Hallmark IFN alpha response module score for each CD4⁺ T cell subset at T+3 by treatment group. Boxplots are overlaid on the violins, with the middle line representing the median and the box edges indicating the 25th and 75th percentiles. Statistical*

comparison between treatment groups was performed using a Wilcoxon rank-sum test. ***B)*** *Volcano plots showing pseudobulk edgeR differential gene expression analysis comparing ruxolitinib and placebo treatment groups at T+7 and rT+3 within the Tr1, Tfh and Th1 cell clusters. Genes with P<0.05 are highlighted, blue indicates upregulation in placebo-treated and red indicating upregulation in ruxolitinib-treated groups. Genes with log2 fold change >1 are labelled.* ***C)*** *Waterfall plots showing single cell pathway analysis (SCPA) for Tr1, Tfh and Th1 cells at T+7 and rT+3 using the Hallmark gene sets.*

Th1, Tfh and Tr1 cells share clonal relationships and can be tracked over the course of first and second infection

Finally, to dissect the relationships and expansion of the Th1, Tfh and Tr1 cells at the clonal level within *P. falciparum*-specific cells, we examined $CD4^+$ T cell subsets and clonal dynamics within the AIM assay dataset. AIM^+ cells were selected from the integrated scRNAseq dataset (Figure 5B) and taken forward for clustering and cell annotation. Clustering of AIM^+ cells identified eight transcriptionally distinct $CD4^+$ T cell subsets; Th1 cells were defined based on expression of *IFNG*, *GNLY*, *GZMK*, *GZMB*; Tfh cells by expression of *CXCR5*, *ICOS* and *CXCL13*; Tr1 cells by expression of *IL10*, *LAG3*, and *PDCD1*. As seen in unstimulated $CD4^+$ T cells, there was significant sharing of transcriptional signatures across Th1, Tfh and Tr1 cells, with Tr1 cells co-expressing Th1- and Tfh cell-associated transcripts, including *IFNG*, *GZMB*, and *ICOS*, *CXCL13* (Fig. 7A-B, Supplementary Fig. 10A-C). Other identified $CD4^+$ T cell subsets included: Th17 cells defined by expression of *IL22* and *IL17A*; T regulatory (Treg) cells that expressed *FOXP3*; Th2 cells identified by expression of *IL4* and *IL5;* a cluster enriched for type I IFN stimulated genes (annotated ISGs) including *CXCL10*, *IFI27* and *IFIT1;* and a cluster expressing *KLF2*, *TLR3*, *ALOX5*, consistent with an activated $CD4^+$ T cell phenotype (Fig. 7A-B). The relative expansion of Th1, Tfh and Tr1 cells in response to *P falciparum* infection was detected at T+7 and subsequent timepoints (Supplementary Fig. 10D).

Within the *ex vivo* and AIM^+ data sets, complete TCRA/B pairs were captured for 62% of cells (88,276 cells, 73,514 unique clonal types). Within the AIM^+ data set, clonal expansion was most evident at T+7 and rT+3, consistent with major activation of parasite-specific $CD4^+$ T cells at these timepoints in first and second infection (Fig. 7C). At these two timepoints, clonal expansion was seen across $CD4^+$ T cell subsets, but was highest in Tr1, Tfh and Th1

533 cells, consistent with these being dominant *P. falciparum*-specific CD4$^+$ T cell subsets (Fig.
534 7D). Expanded clones in the AIM$^+$ data set were detected across donors and could be traced
535 between first and second infection (Fig. 7E). Using an antigen-specific, personalised TCR
536 reference database approach (Marina-Zárate et al., 2025), expanded clones (≥2 cells with
537 shared TCRA/B sequences) identified within the AIM$^+$ dataset were classified as *P.*
538 *falciparum*-specific. We then leveraged these clonotypes to mine the unstimulated *ex vivo*
539 TCR dataset, allowing identification of malaria-specific clones without perturbing cell
540 transcriptional state. This approach detected 1110 *P. falciparum*-specific CD4$^+$ T cells in the
541 *ex vivo* data, across 455 unique clones; these could be tracked across time and between first
542 and second infections (Fig. 7F). Within *ex vivo* data, clonal expansion of these parasite-
543 specific clones was largest at T+7 and rT+3 across donors (Fig. 7G-H). Further, these
544 expanded clones were dominated by Th1, Tfh, Tr1 and cycling cell subsets particularly at
545 T+7 and rT+3, with indications these *P. falciparum*-specific, clonally expanded cells were
546 higher in ruxolitinib-treated participants (Fig. 7G, Supplementary Fig. 10E). Th17 cells
547 accounted for a substantial proportion of AIM$^+$ cells across all timepoints, regardless of
548 treatment (Fig. 7H). However, given the existence of these cells prior to malaria infection and
549 limited change in their frequency over the course of first and second infection, it is likely they
550 represent cytokine responsive, rather than antigen-specific cells, as recently reported in AIM
551 assays for SARS-CoV-2- and influenza-specific CD4$^+$ T cells (Zheng et al., 2025). Within
552 parasite-specific clones, Jaccard index analysis indicated there was clear evidence of clonal
553 sharing across Th1, Tfh and Tr1 cells, and within *ex vivo* data, clones within these subsets
554 overlapped with cycling cells (Fig. 7I-J). Indeed, analysis of clonal subset fidelity indicated
555 that amongst the most highly expanded *P. falciparum*-specific clones (≥5 cells per clone),
556 clones were detected across Tr1, Th1 and Tfh cell subsets in both AIM$^+$ and *ex vivo* data sets
557 (Fig. 7K). This finding was further supported by analysis of individual clones in both data
558 sets, where individual clones were detected in multiple clusters in both AIM$^+$ or *ex vivo* data
559 sets, either at a single timepoint, or across time (Fig. 7L). Taken together, these data reveal
560 enhanced expansion of malaria-specific CD4$^+$ T cells following a second infection and
561 plasticity within Th1, Tfh and Tr1 cells.

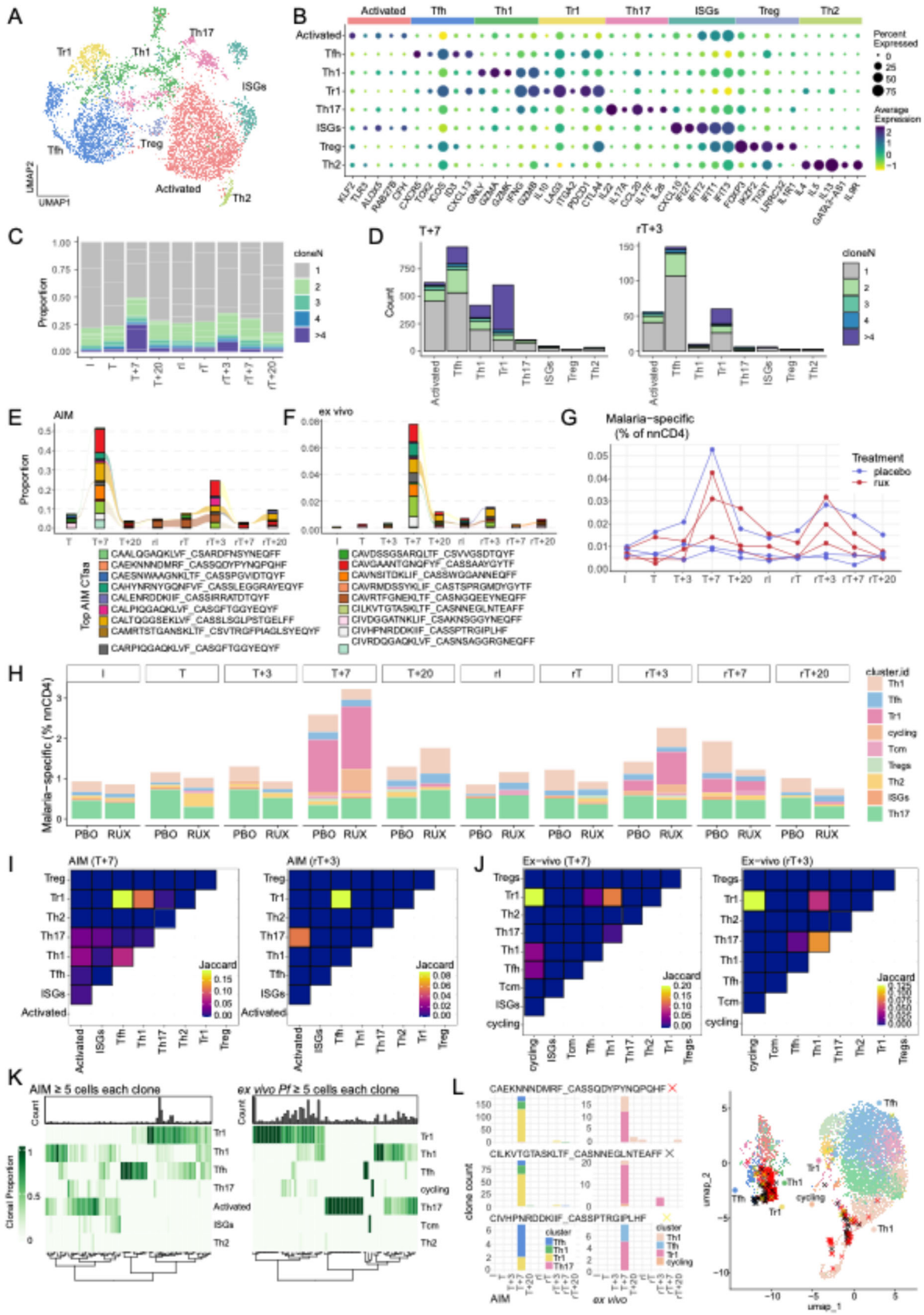

Figure 7: TCR clonal sharing between Th1-Tfh-Tr1 cells in primary and recall responses.

564 ***A)*** *UMAP visualisation showing the AIM cells after integration by donor.* ***B)*** *Dot plot*
565 *showing the average expression of curated marker genes for each AIM cell cluster.* ***C)***
566 *Proportion of cells in each clone family size at each timepoint.* ***D)*** *Clonal family size count*
567 *over time in each subset.* ***E/F)*** *Top 3 expanded P. falciparum-specific clones from each*
568 *participant identified in AIM data set, in AIM* ***(E)*** *and within the ex vivo* ***(F)*** *data sets*
569 *overtime.* ***G)*** *Frequency of P. falciparum-specific cells identified within ex vivo data set, for*
570 *each participant by treatment group.* ***H)*** *P. falciparum-specific cells within ex vivo data set*
571 *across time, within each subset by treatment group.* ***I/J)*** *Clonal overlap amongst P.*
572 *falciparum-specific clones within AIM (****I****) or ex vivo* ***(J)*** *data sets expressed as Jaccard index.*
573 ***K)*** *Clonal subset fidelity of highly expanded clones (≥5 cells per clone). Individual clones are*
574 *in each column with distribution across subsets shown for AIM$^+$ (left) and ex vivo (right)*
575 *data.* ***L)*** *The three top expanded P. falciparum-specific clones are shown with subset fate*
576 *indicated in bars across timepoints for AIM$^+$ and ex vivo data, as indicated (left) or on the*
577 *UMAP of integrated AIM$^+$ and ex vivo data (right). See also Supplementary Figure 10.*

578

579 **Discussion**

580 This study provides a comprehensive phenotypic and transcriptional assessment for how
581 transient JAK1/2 inhibition with ruxolitinib reshapes human CD4$^+$ T cell immunity during
582 controlled human malaria infection. Data reveals that host-directed therapy can alter the
583 quality, kinetics, and durability of anti-parasitic CD4$^+$ T cell responses. Although ruxolitinib
584 transiently suppressed type I IFN signalling and delayed the emergence of highly activated
585 Tr1 cell subsets during first infection, this limited suppression did not impair the development
586 of anti-parasitic immunity. Instead, ruxolitinib treatment altered the CD4$^+$ T cell response,
587 preserving broader signalling pathways, enhancing formation and recall of germinal centre-
588 associated Tfh cells, and driving more pro-inflammatory transcriptional programs across Th1,
589 Tfh and Tr1 cells. Clonal tracking demonstrated that these effects translated into more robust
590 expansion and sustained persistence of *P. falciparum*-specific CD4$^+$ T cell clones following a
591 second infection. These findings show that short-course JAK/STAT inhibition can modulate
592 inflammatory signals during acute infection while simultaneously augmenting the quality of
593 immunological recall responses, thus identifying a promising strategy to stimulate better and
594 more durable vaccine or drug-induced protection against malaria.

595 A primary goal of our host-directed strategy was to transiently limit the development of Tr1
596 cells in volunteers infected with *P. falciparum* following anti-parasitic drug treatment in a
597 first infection. We and others have previously reported that co-inhibitory receptor expression
598 among Tr1 cells is highly variable, both in terms of receptor type and expression level
599 (Brockmann et al., 2018; Edwards et al., 2023). We found that the development of co-
600 inhibitory receptor-rich Tr1 cells was most affected by ruxolitinib treatment. This was not
601 unexpected given the existence of an autologous, type I IFN-dependent pathway for Tr1 cell
602 development, which regulates co-inhibitory receptor expression and IL-10 production (Wang
603 et al., 2023). The therapeutic effect of ruxolitinib on target type I IFN signalling in children
604 with interferonopathies (Fremond et al., 2016) and in patients with dermatomyositis (Ladislau
605 et al., 2018) supports our findings and extends the impact of this drug to type I IFN-mediated
606 Tr1 cell development. The transient nature of this effect further suggests that transiently
607 delaying Tr1 cell expansion does not increase the risk of excessive inflammation, supported
608 by our clinical observations (Webster et al., 2025).

609 The spleen is a key secondary lymphoid tissue during malaria and is composed of the red
610 pulp, which filters blood and removes damaged and infected erythrocytes, and the white pulp,
611 which orchestrates adaptive immune responses (Mebius and Kraal, 2005). Within the white
612 pulp, periarteriolar lymphoid sheaths (PALS) enriched for T cells, B cell follicles that initiate
613 germinal centre reactions, and the marginal zone that captures blood-borne antigens, together
614 form a specialised, compartmentalised architecture that supports coordinated immune
615 activation (Bronte and Pittet, 2013). This organisation is maintained by an intricate network
616 of stromal cells, including fibroblastic reticular cells, follicular dendritic cells, marginal zone
617 stromal cells, and endothelial cells, which provide essential structural scaffolding, organise
618 chemokine gradients such as CCL19, CCL21, and CXCL13, and guide the migration,
619 positioning, and interactions of lymphocytes and antigen-presenting cells (Cupedo et al.,
620 2004; Mueller and Germain, 2009). During acute inflammation, however, excessive cytokine
621 production, tissue-remodelling enzymes, and altered chemokine expression can destabilise
622 these stromal networks, collapse microanatomical niches, and disrupt the boundaries between
623 T and B cell zones (Auffray et al., 2007). In malaria, parasites accumulate in the spleen (Kho
624 et al., 2021), and inflammatory remodelling can impair cell trafficking, weaken germinal
625 centre formation, and reduce the efficiency of T and B cell cooperation (Cadman et al., 2008;
626 Ryg-Cornejo et al., 2016; Urban et al., 2005), underscoring the importance of preserving
627 splenic architecture for effective anti-parasitic immunity. In this context, our findings suggest

628 that in addition to its direct suppression of $CD4^+$ T cell signalling and Tr1 cell differentiation,
629 ruxolitinib may act indirectly by stabilising the lymphoid microenvironment. The capacity of
630 ruxolitinib to reduce acute systemic inflammation during first infection (Webster et al.,
631 2025), likely dampens inflammatory stress on splenic stromal cells, thereby preserving the
632 structural and chemokine cues required for optimal Th1 and Tfh cell support, as has been
633 observed in other inflammatory settings (Alexandre and Mueller, 2018; Gommerman and
634 Browning, 2003). Acute malaria imposes substantial metabolic and transcriptional constraints
635 on T cells within secondary lymphoid tissues, limiting their expansion, survival, and
636 differentiation (Boyle et al., 2024; Vijay et al., 2020). By transiently reducing acute
637 inflammatory responses, ruxolitinib may mitigate this disruption, maintaining functional
638 splenic niches that enable enhanced cycling, prolonged activation, and increased clonal
639 persistence of Th1 and Tfh cells during second infection. This model reconciles the early
640 inhibition of highly activated Tr1 cell development in first infection and the later
641 amplification of Th1 and Tfh cell recall responses, particularly in second infection,
642 suggesting that transient JAK/STAT inhibition functions not only as a direct
643 immunomodulator but also as a microenvironmental stabiliser that promotes more durable
644 anti-parasitic $CD4^+$ T cell immunity.

645 $CD4^+$ T cells exhibit developmental plasticity during infection, enabling them to adopt or
646 transition between effector, regulatory, and helper states in response to dynamic
647 inflammatory and tissue-derived cues (Gagliani and Huber, 2017; O'Shea and Paul, 2010).
648 Therefore, Th1, Tfh, and Tr1 cells can share transcriptional programs, co-express lineage-
649 defining molecules and interconvert depending on antigen load, cytokine exposure, metabolic
650 stress, as well as the microanatomical niche in which they reside (Crotty, 2019).
651 Inflammatory mediators such as type I interferons, IFNγ, IL-10, IL-12, and costimulatory or
652 coinhibitory interactions can redirect differentiation trajectories, allowing $CD4^+$ T cells to
653 fine-tune their function as immune and tissue demands change (Masopust et al., 2025; Tuzlak
654 et al., 2021). In malaria, this plasticity is well documented, and $CD4^+$ T cells frequently
655 display overlapping Th1, Tfh and Tr1 cell phenotypes, co-expressing IFN-γ, IL-10, and
656 CXCR5, and shifting between inflammatory, regulatory, and B cell-helping roles as infection
657 progresses (Boyle et al., 2024; Kurup et al., 2019). IL-10–producing Th1 cells generated
658 during acute *P. falciparum* or *P. berghei* ANKA infection can acquire Tfh cell-like features
659 and migrate into B cell follicles, while Tfh cells themselves may adopt Th1 or Tr1 cell
660 characteristics under strong inflammatory pressure (Edwards et al., 2023; Obeng-Adjei et al.,

661 2015; Ryg-Cornejo et al., 2016). Such plasticity likely helps balance parasite control with
662 limiting immunopathology, though it may also compromise germinal centre responses in
663 severe malaria (Boyle et al., 2024). Our results support this model by demonstrating plasticity
664 within Th1, Tfh and Tr1 cells at both transcriptional and phenotypic levels. Rather than
665 forming discrete, terminally differentiated subsets, these lineages shared transcriptional
666 signatures, overlapping effector modules, and clonal relationships, consistent with dynamic
667 interconversion during infection. This plasticity likely reflects adaptation to distinct
668 microenvironmental cues encountered within specific tissue niches, particularly the spleen,
669 where malaria-induced remodelling generates spatially and temporally heterogeneous
670 cytokine and antigen landscapes (Engwerda et al., 2005; Kho et al., 2021). (Kumar et al.,
671 2019; Wykes and Lewin, 2018)These findings suggest that the fate of anti-parasitic $CD4^+$ T
672 cell subsets is not pre-set but continuously moulded by their microenvironment, highlighting
673 opportunities to modulate T cell states therapeutically to enhance protective immunity.

674 Previous studies on $CD4^+$ T cells from Ugandan children living in a high, perennial malaria
675 transmission region found Tr1 cells were the dominant $CD4^+$ T cell subset after *P. falciparum*
676 infection (Nideffer et al., 2025). These cells were capable of long-term, parasite-specific
677 recall responses and scRNA/TCR sequencing indicated phenotypic clonal fidelity. In
678 contrast, in our CHMI cohort we observe extensive TCR clonal sharing across Th1, Tfh and
679 Tr1 cell subsets, with individual parasite-specific clones spanning different transcriptional
680 and phenotypic states over time. Several biological and experimental factors likely account
681 for these differences. First, Ugandan children and adults experience repeated natural
682 infections over years, potentially generating highly imprinted, long-lived memory clones that
683 appear to have stable Tr1 cell fates, whereas our malaria-naïve volunteers were sampled
684 during primary and very early second infections after rapid parasite clearance, when $CD4^+$ T
685 cells are still transitioning between effector, B cell helping and regulatory states. Second, we
686 deliberately perturbed type I IFN–JAK/STAT signalling with ruxolitinib, altering
687 inflammatory cues and likely promoting dynamic repositioning of Th1, Tfh and Tr1 cell
688 clones rather than reinforcing a single dominant Tr1 cell fate. Third, there are methodological
689 differences: Nideffer *et al.* focused on relatively late, memory timepoints after substantial
690 clonal expansion within well-defined memory subsets enabling a call of "clonal fidelity"
691 (Nideffer et al., 2025), whereas our clone tracking included both *ex vivo* and AIM^+ cells
692 across acute and recall phases, capturing intermediate and mixed transcriptional states that
693 would register as phenotypic heterogeneity rather than fidelity. Together, these distinctions

694 suggest that high-fidelity Tr1 cell imprinting may be a hallmark of long-standing, naturally
695 acquired malaria immunity in endemic settings, while in early infection and under targeted
696 cytokine pathway modulation, malaria-specific $CD4^+$ T cell clones remain highly plastic and
697 redistribute across Th1, Tfh and Tr1 cell compartments.

698 Tfh cells play an important role in helping B cells produce parasite-specific antibodies
699 necessary for effective parasite clearance (Boyle et al., 2024; Chan et al., 2022; Chan et al.,
700 2020). Notably, in addition to promoting the expansion of Tr1 cells following a second
701 infection (including those exhibiting Tfh cell characteristics), ruxolitinib treatment also led to
702 expansion of Tfh1 cells, a subset critical for antibody production in viral infections such as
703 HIV (Baiyegunhi et al., 2018), SARS-CoV-2 (Gong et al., 2020), and influenza (Bentebibel
704 et al., 2013). Recent work has also shown that some subsets of Tfh1 cells associate with
705 antibody development in controlled human malaria infection, together with Tfh2 cells (Soon
706 et al., 2025). Ruxolitinib treatment also resulted in expansion of Tfh-Tr1 cells which shared
707 phenotypes of both subsets. The implications of this shift in Tfh subset dynamics remain
708 unclear, particularly as we found that despite improved control of parasite growth in all
709 participants following a second infection, relative to the first infection, there was no
710 ruxolitinib-mediated improvement (Webster et al., 2025). Nevertheless, changes to Tfh cell
711 subsets may impact on the quality and quantity of the B cell and humoral response, and
712 investigating these changes is the focus of ongoing research endeavours.

713 There are several limitations with our studies, including that it was conducted in malaria-
714 naïve adults in Australia and treatment was administered relatively early during infection due
715 to ethical constraints. Both these factors may have limited our ability to detect differences in
716 parasite growth between participants treated with ruxolitinib and control, following second
717 infection. Additionally, we were unable to establish how ruxolitinib would impact pre-
718 existing anti-parasitic $CD4^+$ T cells. Thus, a logical extension for this work would be to test
719 ruxolitinib as a host-directed treatment in participants in an endemic setting, either during
720 controlled human malaria or in natural infection, assessing influences on parasite control and
721 development of immunity.

722 Together, these findings highlight the potential of transient JAK/STAT inhibition as a
723 rational host-directed strategy to improve $CD4^+$ T cell immunity during acute infection,
724 balancing necessary suppression of early inflammation with enhanced generation of durable,
725 high-quality anti-parasitic memory. By demonstrating that ruxolitinib can modulate $CD4^+$ T
726 cell signalling, delay regulatory skewing, potentially stabilise lymphoid microenvironments,

727 and ultimately amplify recall responses by Th1, Tfh and Tr1 cells, our work provides early
728 evidence for a strategy of deploying immune modulators to compliment other malaria control
729 strategies. Importantly, these insights extend beyond malaria, offering new knowledge for
730 how short-course cytokine pathway inhibition might be used to optimise vaccine- or drug-
731 induced immunity in other infectious diseases characterised by acute inflammatory responses.
732 Future studies in malaria endemic populations, incorporating longer-term clinical endpoints
733 and evaluation of humoral and cellular protective correlates, will be essential to determine
734 whether ruxolitinib or similar agents can safely enhance protective immunity in malaria
735 endemic settings.

736 **Materials and Methods**

737 ***Ethics statement***

738 Ethics approval for this study was obtained from the QIMRB Berghofer Human Research
739 Ethics Committee (P3696 and P1479), and the Alfred Health Ethics Committee (288/23).
740 Written informed consent was obtained from all study participants.

741 ***Study cohort***

742 Samples in this study were collected from a controlled human malaria infection cohort "A
743 randomised, double blind, placebo-controlled trial to evaluate the safety, tolerability and anti-
744 parasitic immunity boosting activation of ruxolitinib when co-administered with artemether-
745 lumenfantrine in healthy volunteers with *Plasmodium falciparum* Induced Blood Stage
746 Malaria". The study is registered with the Australian New Zealand Clinical Trials Registry:
747 ACTRN12621000866808. Study participants were healthy malaria-naïve adults aged 18 to 55
748 years who met the eligibility criteria (Webster et al., 2025).

749 Details of the study design are reported elsewhere (Webster et al., 2025). In brief, in the first
750 phase of the study, 20 participants were intravenously inoculated with 3D7 *P. falciparum*-
751 infected RBCs. Blood parasitemia was monitored from day 4 post-infection using qPCR, and
752 on day 8 or 9 participants were randomised to receive artemether-lumefantrine (AL) with
753 either ruxolitinib or placebo. Participants and investigators were blinded to treatment
754 allocation. 15 participants returned for the second phase of the study and were re-inoculated
755 with *P. falciparum*-infected RBCs 91 days post initial infection, and their blood parasitemia
756 levels monitored as before. AL only was then administered once blood parasitemia levels
757 reached or exceeded 50,000 parasites/ml. One of the participants contracted SARS-CoV-2
758 during the re-infection period and was therefore excluded from subsequent analyses.

759 Participants were monitored to ensure safety and parasite clearance up until six months post
760 initial infection. Blood samples for immunological analyses were collected on designated
761 days throughout the trial.

762 Whole blood from the study participants was collected into lithium heparin tubes and
763 processed for whole blood assays or PBMCs were isolated with Ficoll-Paque (Sigma, USA),
764 density gradient centrifugation. PBMCs were stored in cryopreservation media (90% (v/v)
765 FBS, 10% (v/v) DMSO) in liquid nitrogen storage.

766 ***Whole blood phospho-CYTOF***

767 Whole blood samples were collected from the participants in the clinical trial at day 0
768 (baseline), at pre-treatment on day 8/9, on the second day of treatment day 9/10 (T+1.5, halfway
769 through the treatment regimen) and day 13/14 (T+5, 5 days after the final treatment). Two
770 hundred µl of whole blood (from lithium-heparin) was stimulated with 1µg/ml IFNβ or 50
771 ng/ml IL-2 or 50 ng/ml PMA and 0.4855 µg/ml Ionomycin, or left untreated for 15 min at room
772 temperature, and then fixed with Proteomic Stabilizer (Smart Tube, Inc.) and kept at -80°C.
773 CyTOF was performed by the Human Immune Monitoring Center (HIMC) at Stanford
774 University. Fixed samples were thawed; samples were washed with Smart Tube Thaw-Lyse
775 buffer twice and washed with Cell Staining Buffer (CSB; Standard BioTools) once. The
776 samples where then washed twice with perm buffer (Invitrogen 10× permeabilization buffer
777 #00-8333-56, diluted to 1× in phosphate-buffered saline [PBS] from Standard BioTools). The
778 samples were then resuspended in 900 µl perm buffer and 10 µl of each Standard BioTools
779 CellID 20plex Pd barcode was added before incubating at room temperature for 30 min. Next,
780 the samples were centrifuged, aspirated, and washed three times by resuspension in CSB. The
781 pellets were then resuspended in 450 µl CSB and pooled into a single tube. After centrifugation
782 and aspiration, the pooled sample was counted on a Bio-Rad TC20 cell counter. Surface
783 cocktail was added at 1 test, 20 µl per 1 million counted cells and stained at room temperature
784 for 30 min (Supplementary Table S1). This cocktail was combined from two -80 °C frozen
785 cocktails (HIMC surface stain and Boyle surface stain) to which fresh 143Nd-CD45RA
786 (Standard BioTools) was added. Next, the sample was washed twice by resuspension with
787 CSB. For fixation, 4% paraformaldehyde (PFA) in PBS was added and incubated for 10 min
788 at room temperature before adding PBS to 10 ml, centrifugation, and aspiration. Then, 1 ml of
789 -20°C cold methanol was added and the sample placed at -80°C overnight. The next day, the
790 sample was centrifuged and the methanol aspirated before resuspension in 10 ml PBS and the
791 centrifugation and aspiration repeated. The sample was resuspended in 1 ml CSB and counted

792 by TC20 cell counter. Intracellular cocktail was added: 1 test, 20 µl per 1 million counted cells
793 and stained at room temperature for 30 min. This cocktail was combined from two -80°C frozen
794 cocktails (HIMC intracellular stain and Boyle intracellular stain). After staining, the sample
795 was washed twice with CSB, centrifuged, and aspirated. The pellet was then resuspended in
796 2% PFA/PBS containing 250 nM Ir intercalator (Standard BioTools) and incubated for 20 min
797 at room temperature. Cells were washed once with CSB and twice with MilliQ water. On the
798 same day as staining was finished, cells were diluted to 750 000/ml in MilliQ water containing
799 10× diluted EQ4 normalization beads (Standard BioTools) and acquired by CyTOF, Helios,
800 CyTOF model 3. Data analysis was performed using FlowJo v10 by gating on intact cells based
801 on the iridium isotopes from the intercalator, then on singlets by Ir191 versus cell length
802 followed by cell clustering analyses. No live-dead was used as the sample was fresh complete
803 whole-blood. For clustering analyses, data was batch corrected using the cyCombine package
804 (Pedersen et al., 2022), clustered using FlowSOM (Van Gassen et al., 2015), and annotated by
805 expression profiles of lineage markers on R version 4.3.3. For CD4 T cell subset analysis, CD4
806 T cells were clustered with FlowSOM (Van Gassen et al., 2015), with CD45RA, CD27, CD38,
807 HLA-DR, CD127 and CD25 and the default settings was used to subcluster the $CD4^+$ T cells
808 with a meta.k value of 15. The data was then subsampled to 5000 cells per participant and
809 visualised using the run.umap function. A clustered heatmap and density plots showing the
810 expression of the clustering markers were used to annotate the clusters. After identification of
811 the $CD4^+$ T cells, the create.sumtable function was used to obtain the frequency of the cells as
812 a percentage of the total $CD4^+$ T cells and the mean signal intensity (MSI) of the
813 phosphorylated proteins on the cells for each stimulation condition.

814 ***PBMC Immunophenotyping CyTOF***

815 This assay was performed in the Human Immune Monitoring Center at Stanford University.
816 PBMCs were thawed in warm RPMI+FBS media containing benzonase, washed twice,
817 resuspended in CyFACS buffer (PBS supplemented with 2% BSA, 2 mM EDTA, and 0.1%
818 sodium azide), and viable cells were counted by Vicell. Cells were added to a U-bottom
819 microtiter plate at 1.5 million viable cells/well and washed once by pelleting and
820 resuspension in fresh CyFACS buffer. The cells were stained for 60 min at room temperature
821 with 50 µl of the following antibody-polymer conjugate cocktail (Supplementary Table S2).
822 This cocktail was combined from two -80 °C frozen cocktails (HIMC surface stain and Boyle
823 surface stain). All antibodies were from purified unconjugated, carrier-protein-free stocks
824 from BD Biosciences, Biolegend, or R&D Systems. The polymer and metal isotopes were

825 from Fluidigm Corporation. The cells were washed twice by pelleting and resuspension with
826 500 µl FACS buffer. The cells were resuspended in 100 µl PBS buffer containing 2 µg/ml
827 Live-Dead (DOTA-maleimide (Macrocyclics) containing natural-abundance indium). The
828 cells were washed twice by pelleting and resuspension with 500 µl PBS. The cells were
829 resuspended in 100 µl 2% PFA in PBS and placed at 4° C overnight. The next day, 500 µl
830 CyFACS was added, and the cells were pelleted. The cells were resuspended in 100 µl
831 eBiosciences permeabilization buffer (1x in PBS) and placed on ice for 45 min before
832 washing once with 500 µl CyFACS. The cells were resuspended in 100 µl iridium-containing
833 DNA intercalator (1:2000 dilution in 1x PBS; Fluidigm) and incubated at room temperature
834 for 20 min. The cells were washed once with 500 µl CyFACS and twice in 500 µl MilliQ
835 water. The cells were diluted to 800 000/ml in MilliQ water containing a 10x dilution of EQ
836 Normalization beads (Fluidigm) before injection into the CyTOF (Fluidigm). $CD4^+$ T cells
837 were identified within PBMC based on expression of all markers and then concatenated.
838 Cells were then clustered according to the expression of the T cell markers (CD45RA, CCR7,
839 CXCR3, CXCR5, CD127, CD25, LAG3 and CD49b) using FlowSOM clustering with the
840 default Spectre settings. As a results of low LAG3 staining, an over-clustering approach was
841 used with a meta.k value of 60 to identify cells expressing LAG3. The data was subsampled
842 to 2,500 cells per sample and visualised using UMAP dimensionality reduction using the
843 run.umap function default Spectre package settings. The 60 $CD4^+$ T clusters were annotated
844 according to the expression of the chemokine and activation markers and heatmap was
845 created using the make.pheatmap function in Spectre. Following clustering, the
846 create.sumtable function was used to generate a summary table of the frequencies of the cell
847 subsets as a percent of the total $CD4^+$ T cell population.

848 ***PBMC, Tr1 and $CD4^+$ T cell co-inhibitory receptor flow cytometry***

849 Cryopreserved PBMCs were thawed in RPMI 1640 (Gibco, Life Technologies), containing
850 10% FBS (heat-inactivated) and 0.02% Benzonase Nuclease (Sigma-Aldrich), and thawed
851 cells counted with a DeNovix Cell Drop FL. PBMCs ($1x10^6$ per sample) were stained with
852 antibodies against LAG3, CCR2, CCR5, TIGIT, and TIM3 (Pre-Stain, Supplementary Table
853 4) along with Human Fc block (Invitrogen, 1/30) in 2% FBS/RPMI (cRPMI) at 37 °C, 5%
854 CO_2 for 1 h. Cells were then stained with Surface Stain antibodies (Supplementary Table 3)
855 in Brilliant Stain Buffer (1/10) diluted in 2% FBS/PBS at 37°C, 5% CO_2 for a further 30 min.
856 Cells were washed twice with PBS and stained with Live/Dead Blue (Invitrogen, 1/1000 in
857 PBS) in the dark at room temperature for 15 min. Cells were washed twice with 2% FBS/PBS

858 and fixed using FoxP3 eBioscience fixative/permeabilization buffer at 4°C in the dark for 30
859 min. Cells were washed twice with FoxP3 eBioscience Permeabilization buffer and stained
860 with intracellular stain (Supplementary Table S3) in permeabilization buffer in the dark, at
861 RT for 30 min. Cells were washed twice with permeabilization buffer and fixed with BD
862 stabilising fixative incubated at room temperature for 10 min. Cells were washed and
863 resuspended 2% FBS/PBS and acquired on the Cytek Aurora 5 flow cytometer. Data were
864 analysed with FlowJo version 10.9.0. Dead cells and doublets were excluded and the $CD3^+$
865 $CD8^-$ $CD4^+$ T cells were gated (Supplementary Figure 5). FCS files containing the CD4+ T
866 cell data were exported and analysed in the R package Spectre (Ashhurst et al., 2022). Data
867 was concatenated and cyCombine batch alignment was performed using the default
868 cyCombine correct.batch.effects function. Tr1 cells were identified as NOT Tregs ($CD127^{low}$
869 $CD25^+$) and then as $LAG3^+$/$CD49b^+$ (Supplementary Figure 5). The Tr1 cells were clustered
870 according to the expression of the T cell markers (CD45RA, CCR7, CXCR3, CXCR5, CCR2,
871 CCR5, TIM3, TIGIT, CD38, ICOS, CTLA-4, PD-1, Ki67 and CD161) using FlowSOM
872 clustering with meta.k value of 10 and the default Spectre settings. The Spectre
873 make.pheatmap function was used to create a heat map to visualise the expression of the
874 markers on the 10 Tr1 clusters and the create.sumtable function used to determine the
875 frequencies of the clusters as a percentage of all Tr1 cells. The Tr1 cells were down sampled
876 to 2,500 cells per sample and dimensionality reduction performed using the run.umap
877 function.

878 ***P. falciparum parasite culture***

879 Packed red blood cells (RBCs, acquired from Australian Red Cross, Melbourne Australia)
880 were infected with the *Plasmodium falciparum* 3D7 parasite strain used in CHMI (68) and
881 cultured at 5% hematocrit in Roswell Park Memorial Institute 1640 media (RPMI)
882 supplemented with AlbuMAX II (0.25%) and heat-inactivated human sera (5%), at 37 °C in
883 1% O_2, 5% CO_2, 94% N_2 gas mixture. Culture media was replaced daily, and parasites
884 monitored by Giemsa-stained blood smears. pRBCs were grown to 15% parasitemia and
885 purified from uninfected RBCs (uRBCs) via magnet separation to enrich mature trophozoite
886 stage pRBCs. Purified pRBCs (>95% purity) were stored at80 °C in Glycerolyte
887 cryopreservant. For use in stimulations, glycerolyte preserved parasites or control uRBCs
888 were thawed by dropwise addition of malaria thawing solution (MTS: 0.6% NaCl in H_20) and
889 incubated at room temperature for 10 min. Parasites were washed in MTS/PBS (phosphate

890 bufferd saline) three times with decreasing solution ratios (1:0, 1:1, 0:1). Following thaw,
891 parasites were intact late stage trophozoites and diluted to 1 x 10^6 pRBC / 50µl.

892 ***Activation Induced Marker (AIM) assay***

893 PBMCs were thawed in RPMI 1640 (Gibco) containing 10% FCS and 0.02% Benzonase and
894 rested for 2 hours at 37°C, 5% CO_2, and then stimulated for 18 hours in 96-well plates in
895 10% FCS/RPMI at 1 x 10^6 cells per well with 50 µl pRBCs or uRBCs (1 x 10^6). Following
896 stimulation, PBMCs were stained with antibodies to LAG3, CD49b and CCR7 (Pre-stain,
897 Supplementary Table 4), in Human Fc block (2% FBS/RPMI) at 37°C, 5% CO_2 for 45 min.
898 Cells were washed and stained with Live/Dead Blue (Invitrogen, Thermo Fisher Scientific,
899 Cat# L23015, 1/1,000 PBS) in the dark at room temperature for 15 min. Cells were washed
900 twice with 2% FBS/PBS and stained with Surface Stain antibodies (Supplementary Table 4 in
901 2% FBS/PBS w room temperature for 15 min. Cells were washed twice with 2% FBS/PBS
902 and fixed with BD Stabilizing fixative at room temperature for 20 min. Cells were then
903 washed twice and resuspended in 2% FBS/PBS and acquired on Cytek Aurora 5 using
904 Spectroflo software. Flow cytometry results were then analysed on FlowJo version 10.9.0.
905 $CD4^+$ T cell subsets identified based on FSC/SSC, Live, $CD14^-/CD19^-/CD3^+/CD4^+$ cells
906 (Supplementary Figure 6), and AIM+ cells identified as $CD69^+/OX40^+$ and boolean gating
907 was used to identify subsets (Supplementary Figure 6). Malaria specific AIM+ cells were
908 calculated as % pRBC AIM+ $CD4^+$ T cells minus % uRBC AIM+ $CD4^+$ T cells. Negative
909 values as a result of background subtraction were set to zero.

910 **Single Cell RNA sequencing and analysis**

911 *Cell isolation*

912 PBMCs from four placebo and four ruxolitinib donors at ten timepoints (Supplementary
913 Table 5) were thawed in RPMI 1640 (Gibco) containing 10% FCS and 0.02% Benzonase.
914 Cells were rested for 2 h in 10% FCS/PBS at 37 °C, 5% CO_2 and then incubated with Fc
915 block for 15 min and surface stained with antibodies listed in Supplementary Table 6 for 30
916 min at 4°C. Cells were washed with 1% BSA/PBS and stained for viability with Sytox Blue
917 (Invitrogen (CA, USA), Cat. # S34857) and sorted on BD FACSAria™III Cell Sorter into
918 1% BSA/PBS. For AIM^+ $CD4^+$ T cells, PBMCS were first stimulated with pRBCs as
919 described for AIM assays, then processed as above for unstimulated samples. AIM^+ $CD4^+$ T
920 cells were identified as $CD4^+CD3^+CD45RA^-OX40^+CD69^+$ cells. As AIM assays were
921 performed across multiple days (two donors per experiment) for logistical reasons, a control

922 PBMC sample (HMI16) was included in each assay to rule out potential batch effects across
923 assays.

924 *10 X Genomics Chromium GEX Library preparation and sequencing*

925 Sorted cells were loaded into each lane of Chromium Next GEM Single Cell 5' Reagent Kit
926 v2 (Ex vivo: 6-7 samples were multiplexed per lane; AIM^+: 17-19 samples were multiplexed
927 per lane) and Gel Bead-in- Emulsion (GEMs) generated in the 10X Chromium Controller
928 (Chromium Next GEM Single Cell 5' Kit v2, PN-1000263, Chromium Single cell V(D)J
929 Amplification Kits: Human TCR, PN-1000252, Chromium Next GEM Chip K Single Cell
930 Kit, PN-1000286, Dual Index Kit TT Set A, PN-1000215). 5' Gene Expression Libraries and
931 VDJ libraries (TCR) were generated according to the manufacturer's instructions. Generated
932 libraries were sequenced in an Illumina NextSeq 2000 System using P3 flow cells according
933 to the manufacturer's protocol using paired-end sequencing with the following parameters
934 Read 1: 26 cycles, i7 index: 10 cycles, i5 index: 10 cycles and Read 2: 90 cycles.

935 *Demultiplexing and analysis*

936 Each scRNAseq data set was demultiplexed, aligned and quantified using Cell Ranger
937 software (version 6.0.1;10x Genomics) against the human reference genome (GRCh38-3.0.0)
938 with default parameters. Cells were first demultiplexed using the *HTODemux()* function in
939 Seurat based on sample hashtag oligo (HTO) information. To further confirm donor identity,
940 genotype-based demultiplexing was performed using *cell-snp lite* (version 1.2.2) (Huang and
941 Huang, 2021) to call SNPs from 1000_Genome_Project (Auton et al., 2015) reference panel,
942 followed by *Vireo* (version 0.2.0), in Python (version 3.6.1), to assign each cell to the original
943 donor based on haplotype ratios (Huang et al., 2019). Only cells predicted as singlets were
944 retained for downstream analysis. Cell ranger count matrices for each sample were loaded,
945 merged and analysed using the Seurat package (version 5.1.0) (Hao et al., 2024). Cells were
946 filtered to remove those expressing fewer than 200 genes and more than 6000 genes, and
947 those with more than 5% mitochondrial content. Only genes expressed in three or more cells
948 were considered. TRA/TRB gene expression were removed from the GEX dataset, as well as
949 a small population of contaminating $CD8^+$ T cells and monocytes, prior to further
950 downstream processing.

951 Dataset was split by donor and then each individual donor dataset was normalised by
952 'SCTransform.v2' with regression of mitochondrial mapping percentage. Harmony
953 integration was then performed using the *IntegrateLayers()* function to correct for inter-donor

954 batch effects. Principal component analysis (PCA) was performed using *RunPCA()* and the
955 top 30 principal components were used to compute UMAP visualisation using *RunUMAP()*.

956 *Cell cluster annotation*

957 Clustering and cell annotation were performed separately for the *ex vivo* and AIM datasets.
958 The integrated dataset was first divided by assay (*ex vivo* and AIM), and each dataset was
959 processed independently by performing SCTransform normalisation, Harmony integration by
960 donor, PCA dimensionality reduction and UMAP visualisation as described above. The AIM
961 dataset included samples from only six donors, as two donors were excluded due to technical
962 limitations. *FindNeighbors()* was run using the top 30 principal components and
963 *FindClusters()* was used to perform unsupervised clustering at a resolution of 1- 1.2 (*ex vivo*
964 dataset) or 0.5 (AIM dataset). Cluster marker genes were identified using *FindMarkers()* and
965 clusters were annotated and merged based on canonical cluster marker expression, with ten
966 and eight cell subsets identified for the *ex vivo* and AIM datasets, respectively. The Upset
967 plot was generated using the UpSetR package (Conway et al., 2017) (version 1.4.0) to look at
968 intersections of differentially expressed cluster marker genes between $CD4^+$ T cell subsets.

969 *Gene signature scoring*

970 The Seurat *AddModuleScore()* function was used to calculate gene signatures.

971 *Pseudobulked Differential Gene Expression Analysis and Pathway Analysis*

972 For each cluster (Tr1, Tfh, Th1) and timepoint (T+7, rT+3) raw count data and metadata were
973 extracted from the Seurat objects. Counts were aggregated per donor to generate pseudobulk
974 expression profiles for each cluster and timepoint. Differential expression analysis was
975 performed using edgeR (version 4.6.2) (Chen et al., 2025). Raw counts were supplied to
976 *DGEList*, and normalised using the TMM method (*calcNormFactors*), and dispersions
977 estimated. Quasi-likelihood (QL) F-tests were performed using *glmQLFit* and *glmQLFTest* to
978 identify genes differentially expressed between ruxolitinib- and placebo-treated groups.
979 Genes with $P < 0.05$ were considered significant. Volcano plots were generated using *ggplot2*
980 (version 3.5.1) and *ggrepel* (version 0.9.6). Pathway enrichment analysis was performed for
981 each cluster and timepoint using the *SCPA* package (Bibby et al., 2022) (version 1.6.2),
982 based on the Hallmark gene sets from MSigDB (Liberzon et al., 2015).

983 *TCRA/B clonal analysis*

984 Annotated TCR sequences were integrated with the single-cell transcriptomics data using the
985 *combineTCR()* and *combineExpression()* functions from scRepertoire (version 2.5.0) (Yang et
986 al., 2025). The CDR3 amino acid sequences were used to call and quantify clones. Only cells
987 with single and complete paired TCRA and TCRB chain were included. Clones were defined
988 as cells sharing identical amino acid sequence in both TCRA and TCRB. Malaria-specific
989 clonotypes were defined as expanded clones (≥2 cells per clonotype) identified within the
990 AIM^+ dataset. These paired TCRA/B clonotypes were cross-referenced against the *ex-vivo*
991 $CD4^+$ T cell data by exact matching of the CDR3 amino acid sequences. Clonal overlap
992 between samples was assessed using the *clonalOverlap()* function in scRepertoire, with
993 similarity calculated using Jaccard's index and visualised on heatmaps.

994 **Statistical analysis**

995 The change in CD4 T cell responses over time from either the inoculation or the treatment
996 timepoint was assessed using log-linear mixed effects models with restricted maximum
997 likelihood (REML) estimation, incorporating a random intercept at the participant level. Prior
998 to log10 transformation and modelling, data were transformed by adding half of the lowest
999 value to the zero values. For changes between the first inoculation and treatment timepoint,
1000 only timepoint was added as a fixed effect. Treatment, timepoint, and their interaction were
1001 included as fixed effects to evaluate how the response differs between treatment groups and
1002 how the change in response over time differs between treatment groups. The change over time
1003 for the ruxolitinib group was assessed using contrasts. Residual bootstrapping for linear mixed
1004 effects models at 5000 iterations was applied to account for potential deviations from normality
1005 in the residuals, ensuring robust and reliable estimates. The analysis was performed in R using
1006 R Studio (version 4.3.1) using the Linear and Nonlinear mixed effects model (nlme) package
1007 (version 3.1-163) and the Fit linear mixed-effects models' package lme4 (version 1.1-35-5).
1008 Non-normal residues were addressed using residual bootstrapping with the boot (version 1.3-
1009 30) and the lmeresampler packages (version 0.2.4). All plots were made with the R package
1010 ggplot2 (Wilkinson, 2011) or ggpubr (version 0.6.0) (Kassambara, 2018).

1011 **Data and code availability**

1012 The raw sequencing data and processed Cell Ranger outputs used in this study have been
1013 deposited in the European Genome Archive data base under accession code
1014 EGAS50000001569.

Code used to analyse scRNAseq data is available at DOI: 10.5281/zenodo.18263999. The processed single cell Seurat objects and flow cytometry files for AIM+ $CD4^+$ T cells and Tr1 $CD4^+$ T cells are available at OSF: DOI 10.17605/OSF.IO/JE7YD.

The pCyTOF whole blood data and PBMC CyTOF data are publicly available at: DOI 10.5281/zenodo.14872946 and 10.5281/zenodo.14873240.

Author contributions

TW, SC, JJM, JSM, BEB, MJB and CRE conceptualised study

LB, JAE, DO FLR, MS, DA, ND, MN, RM, TMF, JH, JL and ML performed experiments and analysed data.

MN, FLR, JE, LB optimised protocols

BEB led the clinical trial.

RW provided project management for the clinical trial.

CRE, MJB, BEB, HM, GO provided supervision

RW, FA, GO and HM managed the logistics of sample collection and processing.

MJB, CRE, BEB, JSM, TW, SC, JJM, JSM provided funding

TW, SC, JJM, JSM, BEB, MJB and CRE conceived and managed the project, analysed the data and wrote the manuscript with feedback from all authors.

Acknowledgments:

QIMR-Berghofer and Burnet Institute acknowledge the traditional custodians of the lands where they are located, the Turrbal and Jagera people of Meanjin, and the Boonwurrung and Wurundjeri Woi-wurrong people of the Kulin Nation, respectively.

RBC and human serum were provided by the Australian Red Cross Blood Bank (Melbourne and Brisbane). We thank the volunteers who participated in the clinical trial; staff at the University of Sunshine Coast clinical trial site; staff at the Queensland Paediatric Infectious Diseases Laboratory (QPID) for conducting the malaria PCR assays; members of the Stanford Human Immune Monitoring Center for technical assistance;

This study was funded by the Australian National Health and Medical Research Council (NHMRC) Ideas Grant to BEB and MJB (GNT2002957). BEB and JSM are supported by

NHMRC Investigator Grants (2016792 and 2016396, respectively); MJB is supported by a Snow Medical Fellowship (2022/SF167) and CSL Centenary Fellowship.

Work in the Stanford Human Immune Monitoring Center was supported by the Gates Foundation [INV-008378]. The conclusions and opinions expressed in this work are those of the author(s) alone and shall not be attributed to the Foundation. Under the grant conditions of the Gates Foundation, a Creative Commons Attribution 4.0 License has been assigned to the Author Accepted version of the manuscript.

Competing interests

All authors report no competing interests.

1055 **References**

1056 Alexandre, Y.O., and Mueller, S.N. (2018). Stromal cell networks coordinate immune response
1057 generation and maintenance. Immunological Reviews *283*, 77-85.
1058 Ashhurst, T.M., Marsh-Wakefield, F., Putri, G.H., Spiteri, A.G., Shinko, D., Read, M.N., Smith, A.L., and
1059 King, N.J.C. (2022). Integration, exploration, and analysis of high-dimensional single-cell cytometry
1060 data using Spectre. Cytometry A *101*, 237-253.
1061 Auffray, C., Fogg, D., Garfa, M., Elain, G., Join-Lambert, O., Kayal, S., Sarnacki, S., Cumano, A., Lauvau,
1062 G., and Geissmann, F. (2007). Monitoring of blood vessels and tissues by a population of monocytes
1063 with patrolling behavior. Science *317*, 666-670.
1064 Auton, A., Brooks, L.D., Durbin, R.M., Garrison, E.P., Kang, H.M., Korbel, J.O., Marchini, J.L.,
1065 McCarthy, S., McVean, G.A., and Abecasis, G.R. (2015). A global reference for human genetic
1066 variation. Nature *526*, 68-74.
1067 Baiyegunhi, O., Ndlovu, B., Ogunshola, F., Ismail, N., Walker, B.D., Ndung'u, T., and Ndhlovu, Z.M.
1068 (2018). Frequencies of Circulating Th1-Biased T Follicular Helper Cells in Acute HIV-1 Infection
1069 Correlate with the Development of HIV-Specific Antibody Responses and Lower Set Point Viral Load.
1070 J Virol *92*.
1071 Bentebibel, S.E., Lopez, S., Obermoser, G., Schmitt, N., Mueller, C., Harrod, C., Flano, E., Mejias, A.,
1072 Albrecht, R.A., Blankenship, D.*, et al.* (2013). Induction of ICOS+CXCR3+CXCR5+ TH cells correlates
1073 with antibody responses to influenza vaccination. Sci Transl Med *5*, 176ra132.
1074 Bibby, J.A., Agarwal, D., Freiwald, T., Kunz, N., Merle, N.S., West, E.E., Singh, P., Larochelle, A.,
1075 Chinian, F., Mukherjee, S.*, et al.* (2022). Systematic single-cell pathway analysis to characterize early
1076 T cell activation. Cell Rep *41*, 111697.
1077 Boyle, M.J., Engwerda, C.R., and Jagannathan, P. (2024). The impact of Plasmodium-driven
1078 immunoregulatory networks on immunity to malaria. Nat Rev Immunol.
1079 Boyle, M.J., Jagannathan, P., Bowen, K., McIntyre, T.I., Vance, H.M., Farrington, L.A., Greenhouse, B.,
1080 Nankya, F., Rek, J., Katureebe, A.*, et al.* (2015a). Effector Phenotype of Plasmodium falciparum-
1081 Specific CD4+ T Cells Is Influenced by Both Age and Transmission Intensity in Naturally Exposed
1082 Populations. J Infect Dis *212*, 416-425.
1083 Boyle, M.J., Jagannathan, P., Bowen, K., McIntyre, T.I., Vance, H.M., Farrington, L.A., Schwartz, A.,
1084 Nankya, F., Naluwu, K., Wamala, S.*, et al.* (2017). The Development of Plasmodium falciparum-
1085 Specific IL10 CD4 T Cells and Protection from Malaria in Children in an Area of High Malaria
1086 Transmission. Front Immunol *8*, 1329.
1087 Boyle, M.J., Jagannathan, P., Farrington, L.A., Eccles-James, I., Wamala, S., McIntyre, T.I., Vance,
1088 H.M., Bowen, K., Nankya, F., Auma, A.*, et al.* (2015b). Decline of FoxP3+ Regulatory CD4 T Cells in
1089 Peripheral Blood of Children Heavily Exposed to Malaria. PLoS Pathog *11*, e1005041.
1090 Brockmann, L., Soukou, S., Steglich, B., Czarnewski, P., Zhao, L., Wende, S., Bedke, T., Ergen, C.,
1091 Manthey, C., Agalioti, T.*, et al.* (2018). Molecular and functional heterogeneity of IL-10-producing
1092 CD4(+) T cells. Nat Commun *9*, 5457.
1093 Bronte, V., and Pittet, M.J. (2013). The spleen in local and systemic regulation of immunity. Immunity
1094 *39*, 806-818.
1095 Cadman, E.T., Abdallah, A.Y., Voisine, C., Sponaas, A.M., Corran, P., Lamb, T., Brown, D., Ndungu, F.,
1096 and Langhorne, J. (2008). Alterations of splenic architecture in malaria are induced independently of
1097 Toll-like receptors 2, 4, and 9 or MyD88 and may affect antibody affinity. Infect Immun *76*, 3924-
1098 3931.
1099 Chan, J.A., Loughland, J.R., de la Parte, L., Okano, S., Ssewanyana, I., Nalubega, M., Nankya, F.,
1100 Musinguzi, K., Rek, J., Arinaitwe, E.*, et al.* (2022). Age-dependent changes in circulating Tfh cells
1101 influence development of functional malaria antibodies in children. Nat Commun *13*, 4159.
1102 Chan, J.A., Loughland, J.R., de Labastida Rivera, F., SheelaNair, A., Andrew, D.W., Dooley, N.L., Wines,
1103 B.D., Amante, F.H., Webb, L., Hogarth, P.M.*, et al.* (2020). Th2-like T Follicular Helper Cells Promote
1104 Functional Antibody Production during Plasmodium falciparum Infection. Cell Rep Med *1*, 100157.

1105 Chen, Y., Chen, L., Lun, Aaron T.L., Baldoni, Pedro L., and Smyth, Gordon K. (2025). edgeR v4:
1106 powerful differential analysis of sequencing data with expanded functionality and improved support
1107 for small counts and larger datasets. Nucleic Acids Research *53*.
1108 Chughlay, M.F., Barnes, K.I., El Gaaloul, M., Abla, N., Mohrle, J.J., Griffin, P., van Giersbergen, P.,
1109 Reuter, S.E., Schultz, H.B., Kress, A.*, et al.* (2022). Safety, Tolerability, Pharmacokinetics, and
1110 Pharmacodynamics of Coadministered Ruxolitinib and Artemether-Lumefantrine in Healthy Adults.
1111 Antimicrob Agents Chemother *66*, e0158421.
1112 Conway, J.R., Lex, A., and Gehlenborg, N. (2017). UpSetR: an R package for the visualization of
1113 intersecting sets and their properties. Bioinformatics *33*, 2938-2940.
1114 Crotty, S. (2019). T Follicular Helper Cell Biology: A Decade of Discovery and Diseases. Immunity *50*,
1115 1132-1148.
1116 Cupedo, T., Jansen, W., Kraal, G., and Mebius, R.E. (2004). Induction of secondary and tertiary
1117 lymphoid structures in the skin. Immunity *21*, 655-667.
1118 Edwards, C.L., Ng, S.S., de Labastida Rivera, F., Corvino, D., Engel, J.A., Montes de Oca, M., Bukali, L.,
1119 Frame, T.C., Bunn, P.T., Chauhan, S.B.*, et al.* (2023). IL-10-producing Th1 cells possess a distinct
1120 molecular signature in malaria. The Journal of clinical investigation *133*.
1121 Engwerda, C.R., Beattie, L., and Amante, F.H. (2005). The importance of the spleen in malaria. Trends
1122 Parasitol *21*, 75-80.
1123 Fremond, M.L., Rodero, M.P., Jeremiah, N., Belot, A., Jeziorski, E., Duffy, D., Bessis, D., Cros, G., Rice,
1124 G.I., Charbit, B.*, et al.* (2016). Efficacy of the Janus kinase 1/2 inhibitor ruxolitinib in the treatment of
1125 vasculopathy associated with TMEM173-activating mutations in 3 children. J Allergy Clin Immunol
1126 *138*, 1752-1755.
1127 Gagliani, N., and Huber, S. (2017). Basic Aspects of T Helper Cell Differentiation. Methods Mol Biol
1128 *1514*, 19-30.
1129 Gommerman, J.L., and Browning, J.L. (2003). Lymphotoxin/LIGHT, lymphoid microenvironments and
1130 autoimmune disease. Nature Reviews Immunology *3*, 642-655.
1131 Gong, F., Dai, Y., Zheng, T., Cheng, L., Zhao, D., Wang, H., Liu, M., Pei, H., Jin, T., Yu, D., and Zhou, P.
1132 (2020). Peripheral CD4+ T cell subsets and antibody response in COVID-19 convalescent individuals.
1133 The Journal of clinical investigation *130*, 6588-6599.
1134 Hao, Y., Stuart, T., Kowalski, M.H., Choudhary, S., Hoffman, P., Hartman, A., Srivastava, A., Molla, G.,
1135 Madad, S., Fernandez-Granda, C., and Satija, R. (2024). Dictionary learning for integrative,
1136 multimodal and scalable single-cell analysis. Nat Biotechnol *42*, 293-304.
1137 Huang, X., and Huang, Y. (2021). Cellsnp-lite: an efficient tool for genotyping single cells.
1138 Bioinformatics *37*, 4569-4571.
1139 Huang, Y., McCarthy, D.J., and Stegle, O. (2019). Vireo: Bayesian demultiplexing of pooled single-cell
1140 RNA-seq data without genotype reference. Genome Biol *20*, 273.
1141 Jagannathan, P., Eccles-James, I., Bowen, K., Nankya, F., Auma, A., Wamala, S., Ebusu, C., Muhindo,
1142 M.K., Arinaitwe, E., Briggs, J.*, et al.* (2014). IFNgamma/IL-10 co-producing cells dominate the CD4
1143 response to malaria in highly exposed children. PLoS Pathog *10*, e1003864.
1144 Kassambara, A. (2018). ggpubr:'ggplot2'based publication ready plots. R package version, 2.
1145 Kho, S., Qotrunnada, L., Leonardo, L., Andries, B., Wardani, P.A.I., Fricot, A., Henry, B., Hardy, D.,
1146 Margyaningsih, N.I., Apriyanti, D.*, et al.* (2021). Hidden Biomass of Intact Malaria Parasites in the
1147 Human Spleen. N Engl J Med *384*, 2067-2069.
1148 Kumar, R., Bunn, P.T., Singh, S.S., Ng, S.S., Montes de Oca, M., De Labastida Rivera, F., Chauhan, S.B.,
1149 Singh, N., Faleiro, R.J., Edwards, C.L.*, et al.* (2020). Type I Interferons Suppress Anti-parasitic
1150 Immunity and Can Be Targeted to Improve Treatment of Visceral Leishmaniasis. Cell Rep *30*, 2512-
1151 2525 e2519.
1152 Kumar, R., Ng, S., and Engwerda, C. (2019). The Role of IL-10 in Malaria: A Double Edged Sword.
1153 Front Immunol *10*, 229.
1154 Kurup, S.P., Butler, N.S., and Harty, J.T. (2019). T cell-mediated immunity to malaria. Nat Rev
1155 Immunol *19*, 457-471.

Ladislau, L., Suarez-Calvet, X., Toquet, S., Landon-Cardinal, O., Amelin, D., Depp, M., Rodero, M.P., Hathazi, D., Duffy, D., Bondet, V.*, et al.* (2018). JAK inhibitor improves type I interferon induced damage: proof of concept in dermatomyositis. Brain *141*, 1609-1621.
Liberzon, A., Birger, C., Thorvaldsdóttir, H., Ghandi, M., Mesirov, J.P., and Tamayo, P. (2015). The Molecular Signatures Database (MSigDB) hallmark gene set collection. Cell Syst *1*, 417-425.
Mandala, W.L., Ward, S., Taylor, T.E., and Wassmer, S.C. (2022). Characterization of Lymphocyte Subsets in Lymph Node and Spleen Sections in Fatal Pediatric Malaria. Pathogens *11*, 851.
Marina-Zárate, E., Sutton, H.J., Lopez, P.G., Altheide, T.K., Bick, M., Burton, I., Ben-Akiva, E., Kaczmarek Michaels, K., Hyacinth, K., Healy, B.S.*, et al.* (2025). Highly functional and prolonged germinal center T follicular helper cell responses are associated with enhanced neutralizing antibody development. Immunity *58*, 3094-3112.e3097.
Masopust, D., Awasthi, A., Bosselut, R., Brooks, D.G., Buggert, M., Chamoto, K., Cui, W., Dong, C., Farber, D.L., Gebhardt, T.*, et al.* (2025). Guidelines for T cell nomenclature. Nat Rev Immunol.
Mebius, R.E., and Kraal, G. (2005). Structure and function of the spleen. Nat Rev Immunol *5*, 606-616.
Moncunill, G., Carnes, J., Chad Young, W., Carpp, L., De Rosa, S., Campo, J.J., Nhabomba, A., Mpina, M., Jairoce, C., Finak, G.*, et al.* (2022). Transcriptional correlates of malaria in RTS,S/AS01-vaccinated African children: a matched case-control study. Elife *11*.
Montes de Oca, M., Good, M.F., McCarthy, J.S., and Engwerda, C.R. (2016a). The Impact of Established Immunoregulatory Networks on Vaccine Efficacy and the Development of Immunity to Malaria. J Immunol *197*, 4518-4526.
Montes de Oca, M., Kumar, R., de Labastida Rivera, F., Amante, F.H., Sheel, M., Faleiro, R.J., Bunn, P.T., Best, S.E., Beattie, L., Ng, S.S.*, et al.* (2016b). Blimp-1-Dependent IL-10 Production by Tr1 Cells Regulates TNF-Mediated Tissue Pathology. PLoS Pathog *12*, e1005398.
Montes de Oca, M., Kumar, R., Rivera, F.L., Amante, F.H., Sheel, M., Faleiro, R.J., Bunn, P.T., Best, S.E., Beattie, L., Ng, S.S.*, et al.* (2016c). Type I Interferons Regulate Immune Responses in Humans with Blood-Stage Plasmodium falciparum Infection. Cell Rep *17*, 399-412.
Morita, R., Schmitt, N., Bentebibel, S.E., Ranganathan, R., Bourdery, L., Zurawski, G., Foucat, E., Dullaers, M., Oh, S., Sabzghabaei, N.*, et al.* (2011). Human blood CXCR5(+)CD4(+) T cells are counterparts of T follicular cells and contain specific subsets that differentially support antibody secretion. Immunity *34*, 108-121.
Mueller, S.N., and Germain, R.N. (2009). Stromal cell contributions to the homeostasis and functionality of the immune system. Nat Rev Immunol *9*, 618-629.
Nahrendorf, W., Ivens, A., and Spence, P.J. (2021). Inducible mechanisms of disease tolerance provide an alternative strategy of acquired immunity to malaria. Elife *10*.
Nideffer, J., Bach, F., Nankya, F., Musinguzi, K., Borna, Š., Mantilla, M., Zedi, M., Garcia Romero, A., Gerungan, C., Yang, N.*, et al.* (2025). Clone tracking through repeated malaria identifies high-fidelity memory CD4 T cell responses. Sci Immunol *10*, eads2957.
Nielsen, C.M., Ogbe, A., Pedroza-Pacheco, I., Doeleman, S.E., Chen, Y., Silk, S.E., Barrett, J.R., Elias, S.C., Miura, K., Diouf, A.*, et al.* (2021). Protein/AS01(B) vaccination elicits stronger, more Th2-skewed antigen-specific human T follicular helper cell responses than heterologous viral vectors. Cell Rep Med *2*, 100207.
O'Shea, J.J., and Paul, W.E. (2010). Mechanisms underlying lineage commitment and plasticity of helper CD4+ T cells. Science *327*, 1098-1102.
Obeng-Adjei, N., Portugal, S., Tran, T.M., Yazew, T.B., Skinner, J., Li, S., Jain, A., Felgner, P.L., Doumbo, O.K., Kayentao, K.*, et al.* (2015). Circulating Th1-Cell-type Tfh Cells that Exhibit Impaired B Cell Help Are Preferentially Activated during Acute Malaria in Children. Cell Rep *13*, 425-439.
Olotu, A., Fegan, G., Wambua, J., Nyangweso, G., Leach, A., Lievens, M., Kaslow, D.C., Njuguna, P., Marsh, K., and Bejon, P. (2016). Seven-Year Efficacy of RTS,S/AS01 Malaria Vaccine among Young African Children. N Engl J Med *374*, 2519-2529.

1206 Oyong, D.A., Duffy, F.J., Neal, M.L., Du, Y., Carnes, J., Schwedhelm, K.V., Hertoghs, N., Jun, S.H.,
1207 Miller, H., Aitchison, J.D.*, et al.* (2023). Distinct immune responses associated with vaccination status
1208 and protection outcomes after malaria challenge. PLoS Pathog *19*, e1011051.
1209 Pedersen, C.B., Dam, S.H., Barnkob, M.B., Leipold, M.D., Purroy, N., Rassenti, L.Z., Kipps, T.J.,
1210 Nguyen, J., Lederer, J.A., Gohil, S.H.*, et al.* (2022). cyCombine allows for robust integration of single-
1211 cell cytometry datasets within and across technologies. Nature Communications *13*, 1698.
1212 Platanias, L.C. (2005). Mechanisms of type-I- and type-II-interferon-mediated signalling. Nat Rev
1213 Immunol *5*, 375-386.
1214 Rogerson, S.J., Wijesinghe, R.S., and Meshnick, S.R. (2010). Host immunity as a determinant of
1215 treatment outcome in Plasmodium falciparum malaria. Lancet Infect Dis *10*, 51-59.
1216 Roncarolo, M.G., Gregori, S., Bacchetta, R., and Battaglia, M. (2014). Tr1 cells and the counter-
1217 regulation of immunity: natural mechanisms and therapeutic applications. Current topics in
1218 microbiology and immunology *380*, 39-68.
1219 Roncarolo, M.G., Gregori, S., Bacchetta, R., Battaglia, M., and Gagliani, N. (2018). The Biology of T
1220 Regulatory Type 1 Cells and Their Therapeutic Application in Immune-Mediated Diseases. Immunity
1221 *49*, 1004-1019.
1222 Ryg-Cornejo, V., Ioannidis, L.J., Ly, A., Chiu, C.Y., Tellier, J., Hill, D.L., Preston, S.P., Pellegrini, M., Yu,
1223 D., Nutt, S.L.*, et al.* (2016). Severe Malaria Infections Impair Germinal Center Responses by Inhibiting
1224 T Follicular Helper Cell Differentiation. Cell Rep *14*, 68-81.
1225 Sallusto, F. (2016). Heterogeneity of human CD4+ T cells against microbes. Annual review of
1226 immunology *34*, 317-334.
1227 Soon, M.S., Oyong, D.A., Dooley, N.L., Mukhiya, R., Pava, Z., Andrew, D.W., Loughland, J.R.,
1228 McCarthy, J.S., Chan, J.A., Beeson, J.G.*, et al.* (2025). Tfh2 and a subset of Tfh1 cells associate with
1229 antibody-mediated immunity to malaria. JCI Insight *10*.
1230 Tubo, N.J., and Jenkins, M.K. (2014). CD4+ T Cells: guardians of the phagosome. Clinical microbiology
1231 reviews *27*, 200-213.
1232 Tuzlak, S., Dejean, A.S., Iannacone, M., Quintana, F.J., Waisman, A., Ginhoux, F., Korn, T., and Becher,
1233 B. (2021). Repositioning TH cell polarization from single cytokines to complex help. Nature
1234 immunology *22*, 1210-1217.
1235 Urban, B.C., Hien, T.T., Day, N.P., Phu, N.H., Roberts, R., Pongponratn, E., Jones, M., Mai, N.T.,
1236 Bethell, D., Turner, G.D.*, et al.* (2005). Fatal Plasmodium falciparum malaria causes specific patterns
1237 of splenic architectural disorganization. Infect Immun *73*, 1986-1994.
1238 Van Gassen, S., Callebaut, B., Van Helden, M.J., Lambrecht, B.N., Demeester, P., Dhaene, T., and
1239 Saeys, Y. (2015). FlowSOM: Using self-organizing maps for visualization and interpretation of
1240 cytometry data. Cytometry A *87*, 636-645.
1241 van Wolfswinkel, M.E., Langenberg, M.C.C., Wammes, L.J., Sauerwein, R.W., Koelewijn, R., Hermsen,
1242 C.C., van Hellemond, J.J., and van Genderen, P.J. (2017). Changes in total and differential leukocyte
1243 counts during the clinically silent liver phase in a controlled human malaria infection in malaria-naïve
1244 Dutch volunteers. Malaria Journal *16*, 457.
1245 Vijay, R., Guthmiller, J.J., Sturtz, A.J., Surette, F.A., Rogers, K.J., Sompallae, R.R., Li, F., Pope, R.L.,
1246 Chan, J.A., de Labastida Rivera, F.*, et al.* (2020). Infection-induced plasmablasts are a nutrient sink
1247 that impairs humoral immunity to malaria. Nature immunology *21*, 790-801.
1248 Walther, M., Jeffries, D., Finney, O.C., Njie, M., Ebonyi, A., Deininger, S., Lawrence, E., Ngwa-
1249 Amambua, A., Jayasooriya, S., Cheeseman, I.H.*, et al.* (2009). Distinct roles for FOXP3 and FOXP3 CD4
1250 T cells in regulating cellular immunity to uncomplicated and severe Plasmodium falciparum malaria.
1251 PLoS Pathog *5*, e1000364.
1252 Wang, Y., De Labastida Rivera, F., Edwards, C.L., Frame, T.C., Engel, J.A., Bukali, L., Na, J., Ng, S.S.,
1253 Corvino, D., Montes de Oca, M.*, et al.* (2023). STING activation promotes autologous type I
1254 interferon-dependent development of type 1 regulatory T cells during malaria. The Journal of clinical
1255 investigation *133*.

Webster, R., Oyong, D.A., Llewellyn, S., Abd-Rahman, A.N., Potter, A.J., Mukhiya, R., Sahai, N., Leelasena, I., Ujvary, E., Mathison, S*., et al.* (2025). Adjunctive ruxolitinib attenuates inflammation and enhances immunity in volunteers experimentally infected with Plasmodium falciparum. Sci Transl Med *17*, eaea2531.

WHO (2025). World malaria report 2025. (Geneva, World Health Organization).

Wilkinson, L. (2011). ggplot2: elegant graphics for data analysis by WICKHAM, H. (Oxford University Press).

Wykes, M.N., and Lewin, S.R. (2018). Immune checkpoint blockade in infectious diseases. Nat Rev Immunol *18*, 91-104.

Yang, Q., Safina, K.R., Nguyen, K.D.Q., Tuong, Z.K., and Borcherding, N. (2025). scRepertoire 2: Enhanced and efficient toolkit for single-cell immune profiling. PLoS Comput Biol *21*, e1012760.

Zander, R.A., Guthmiller, J.J., Graham, A.C., Pope, R.L., Burke, B.E., Carr, D.J., and Butler, N.S. (2016). Type I Interferons Induce T Regulatory 1 Responses and Restrict Humoral Immunity during Experimental Malaria. PLoS Pathog *12*, e1005945.

Zheng, M.Z.M., Burmas, L., Tan, H.-X., Trieu, M.-C., Lee, H.J., Rawlinson, D., Haque, A., Kent, S.J., Wheatley, A.K., and Juno, J.A. (2025). Deconvoluting TCR-dependent and -independent activation is vital for reliable Ag-specific CD4⁺ T cell characterization by AIM assay. Science Advances *11*, eadv3491.

1 *Supplementary Tables and Figures*
2
3 *Supplementary Tables*
4
5 **Supplementary Table S1. pCyTOF whole blood staining panel**

Metal label	Specificity	Clone	Supplier	Cat#	Cocktail
89Y	CD45	HI30	Standard BioTools	3089003B	Boyle surface-frozen
141Pr	CD7	CD7-6B7	Biolegend	343111	HIMC surface-frozen
142Nd	CD19	HIB19	Standard BioTools	3142001B	HIMC surface-frozen
143Nd	CD45RA	HI100	Standard BioTools	3143006B	Boyle surface-liquid drop-in
144Nd	pPLCg2	K86-689.37	Standard BioTools	3144015A	HIMC-intracellular-frozen
145Nd	CD4	RPA-T4	Standard BioTools	3145001B	HIMC surface-frozen
146Nd	IgD	IA6-2	Standard BioTools	3146005B	HIMC surface-frozen
147Sm	CD20	2H7	Standard BioTools	3147007B	HIMC surface-frozen
148Nd	IgA	Polyclonal	Standard BioTools	3148007B	Boyle surface-frozen
149Sm	CD25	2A3	Standard BioTools	3149010B	HIMC surface-frozen
150Nd	pSTAT5	47	Standard BioTools	3150005A	HIMC-intracellular-frozen
151Eu	CD123	6H6	Standard BioTools	3151001B	HIMC surface-frozen
152Sm	Akt	D9E	Standard BioTools	3152005A	HIMC-intracellular-frozen
153Eu	pSTAT1	4a	Standard BioTools	3153005A	HIMC-intracellular-frozen
154Sm	CD127	R34-34	Novus Biological	DDX0700P-100	Boyle surface-frozen
155Gd	CD27	L128	Standard BioTools	3155001B	HIMC surface-frozen
156Gd	pP38	D3F9	Standard BioTools	3156002A	HIMC-intracellular-frozen
158Gd	pSTAT3	4	Standard BioTools	3158005A	HIMC-intracellular-frozen
159Tb	CD11c	Bu15	Standard BioTools	3159001B	HIMC surface-frozen
160Gd	CD14	M5E2	Standard BioTools	3160001B	HIMC surface-frozen
162Dy	CD66b	80H3	Standard BioTools	3162023B	Boyle surface-frozen
163Dy	CD56	NCAM16.2	Standard BioTools	3163007B	HIMC surface-frozen
164Dy	IkBalpha	L35A5	Standard BioTools	3164004A	HIMC-intracellular-frozen
165Ho	CD16	B73.1	Standard BioTools	3167001B	Boyle surface-frozen
167Er	CD38	HIT2	Standard BioTools	3168002B	HIMC surface-frozen
168Er	CD8	SK1	Standard BioTools	3169010B	HIMC surface-frozen
169Tm	CD33	WM53	Standard BioTools	3170001B	Boyle surface-frozen
170Er	CD3	UCHT1	Standard BioTools	3167001B	HIMC surface-frozen
171Yb	pERK 1/2	D13.14.4E	Standard BioTools	3171010A	HIMC-intracellular-frozen
172Yb	Ki67	B56	Standard BioTools	3172024B	Boyle-intracellular-frozen
173Yb	CD21	Bu32	Biolegend	354902	Boyle surface-frozen
174Yb	HLA-DR	L243	Standard BioTools	3174001B	HIMC surface-frozen
175Lu	pS6	N7548	Standard BioTools	3175009A	HIMC-intracellular-frozen
176Yb	CREB	87G3	Standard BioTools	3176005A	Boyle-intracellular-frozen
209Bi	CD11b	ICRF44	Standard BioTools	3209003B	Boyle surface-frozen

6 **Supplementary Table S2: PBMC immunophenotyping CyTOF panel**

Metal label	Specificity	Clone	Supplier	Cat#	Cocktail
113In	CD57	HNK-1	Biolegend	359602	HIMC frozen
115In	live/dead				
141Pr	CCR6	G034E3	Standard BioTools	3141003A	Boyle frozen
142Nd	CD19	SJ25C1	Biolegend	363002	HIMC frozen
143Nd	CD4	SK3	Biolegend	344602	HIMC frozen
144Nd	CD8	SK1	Biolegend	344702	HIMC frozen
145Nd	CD39	A1	Biolegend	328202	HIMC frozen
146Nd	IgD	IA6-2	Biolegend	348202	HIMC frozen
147Sm	CD85j	292319	R&D Systems	MAB20172	HIMC frozen
148Nd	CD11c	Bu15	Biolegend	337202	HIMC frozen
149Sm	CD16	3G8	Biolegend	302002	HIMC frozen
150Nd	CD3	UCHT1	Biolegend	300402	HIMC frozen
151Eu	CD38	HB-7	Biolegend	356602	HIMC frozen
152Sm	CD27	L128	BD Biosciences	special order	HIMC frozen
153Eu	CD21	Bu32	Biolegend	354902	Boyle frozen
154Sm	CD14	M5E2	Biolegend	301802	HIMC frozen
155Gd	Vd2 TCR	B6	Biolegend	331402	Boyle frozen
156Gd	CD94	HP-3D9	BD Biosciences	555887	HIMC frozen
157Gd	CD86	IT2.2	Biolegend	305402	HIMC frozen
158Gd	CXCR5	RF8B2	BD Biosciences	552032	HIMC frozen
159Tb	CXCR3	G025H7	Biolegend	353702	HIMC frozen
160Gd	CCR7	150503	R&D Systems	MAB197	HIMC frozen
162Dy	CD45RA	HI100	Biolegend	304102	HIMC frozen
164Dy	CD20	2H7	Biolegend	302302	HIMC frozen
165Ho	CD127	A019D5	Biolegend	351302	HIMC frozen
166Er	CD33	P67.6	Biolegend	366602	HIMC frozen
167Er	LAG3	11C3C65	Biolegend	369302	Boyle frozen
168Er	CD49b	P1E6-C5	Biolegend	359302	Boyle frozen
169Tm	ICOS	DX29	BD Biosciences	557801	HIMC frozen
170Er	CD161	DX12	BD Biosciences	556079	HIMC frozen
171Yb	TCRgd	B1	Biolegend	331202	HIMC frozen
172Yb	PD-1	EH12.1	BD Biosciences	562138	HIMC frozen
173Yb	CD123	9F5	BD Biosciences	555642	HIMC frozen
174Yb	CD56	NCAM16.2	BD Biosciences	559043	HIMC frozen
175Lu	HLA-DR	G46-6	BD Biosciences	556642	HIMC frozen
176Yb	CD25	M-A251	Biolegend	356102	HIMC frozen
209Bi	CD11b	ICRF44	Standard BioTools	3209003B	Boyle frozen

7

8 **Supplementary Table 3: PBMC CD4 T cells, Tr1 coinhibitory flow cytometry panel**

Target	Flurophor	Clone	Source	Dilution	Catalogue #
Pre-Stain					
LAG3	Alexa Fluor 647	11C3C65	Biolegend	1/50	369304
CCR2	APC-Cy7	K036C2	Biolegend	1/120	357220
CCR5	BV 650	3A9	BD Biosciences	1/80	564999
TIGIT	PE Dazzle	VSTM3	Biolegend		372716
TIM3	BV605	F38-2E2	Thermo Fisher	1/100	16-3109-85
Surface Stain					
CD161	Alexa Fluor 700	HP-3G10	Biolegend	1/200	339942
CD45RA	BUV 563	HI100	BD Biosciences	1/800	565702
CD4	BUV 737	SK3	BD Biosciences	1/120	564305
CD8	BUV 496	RPA-T8	BD Biosciences	1/800	612942
CD3	BUV 805	SK7	BD Biosciences	1/500	612893
CXCR3	BV421	IC6/CXCR3	BD Biosciences	1/100	562558
CD38	BV480	HIT2	BD Biosciences	1/50	566137
CD14	BV510	M5E2	Biolegend	1/100	301842
CD19	BV510	SJ25C1	Biolegend	1/100	363020
CD127	BV570	A019D5	Biolegend	1/50	351308
CXCR5	BV711	J252D4	Biolegend	1/50	356934
ICOS	BV750	C398.4A	Biolegend	1/100	313558
CD49b	FITC	Y418	Invitrogen	1/100	11-0498-42
PD1	PE/Cy7	EH12.1	BD Biosciences	1/100	561272
CD16	PE/Fire 640	3G8	Biolegend	1/200	302068
CD25	PE/Fire 700	M-A251	Biolegend	1/100	356146
CCR7	PerCP Cy5.5	150503	BD Biosciences	1/80	561144
Intra-cellular Stain					
CTLA-4	BV750	BNI3	BD Biosciences	1/120	563931
Ki67	BUV395	B56	BD Biosciences	1/200	564071
NKG7	PE	2G9A10F5	Beckman Coulter	1/2000	IM3293

9

10

11 **Supplementary Table 4: Antigen-induced marker assay flow cytometry panel**

Antibody		**Clone**	**Source**	**Dilution**	**Catalogue Number**
Pre-Stain					
LAG3	BV421	T47-530	BD Biosciences	1/50	565720
CD49b	FITC	Y418	Invitrogen	1/100	11-0498-42
CCR7	PerCP Cy5.5	G043H7	Biolegend	1/25	353220
Surface Stain					
CD161	AF700	HP-3G10	Biolegend	1/50	339942
OX40	APC	ACT35	BD Biosciences	1/50	563473
CD45RA	BUV563	HI100	BD Biosciences	1/400	565702
CD8	BUV496	RPA-T8	BD Biosciences	1/100	612942
CD3	BUV805	SK7	BD Biosciences	1/50	612893
CD69	BUV737	FN50	BD Biosciences	1/100	612817
CD14	BV510	M5E2	Biolegend	1/100	301842
CD19	BV510	HIB19	Biolegend	1/100	302241
CCR4	BV605	L291H4	Biolegend	1/100	359418
CCR6	BV650	11A9	BD Biosciences	1/50	563922
CXCR5	BV711	J252D4	Biolegend	1/50	356934
CD4	BV785	OKT4	Biolegend	1/50	317442
CD25	PE	BC96	Biolegend	1/200	302906
PD1	PE/Cy7	EH12.1	BD Biosciences	1/50	561272

12
13

14 **Supplementary Table 5: scRNAseq participant characteristics and parasitemia at time of**
15 **ruxolitinib or placebo administration. BMI, body mass index.**

	All (n=8)	Ruxolitinib (n=4)	Placebo (n=4)
Male sex, n (%)	4 (50)	3 (75)	1 (25)
Age, years (median, range)	28 (18-39)	35 (21-39)	27 (18-29)
BMI, Kg/m^2 (median, range)	23 (20-31)	26 (20-31)	22 (20-28)
Race white, n (%)	6 (75)	2 (50)	4 (100)
Parasitemia, parasites/ml (geometric mean, range)	15320 (1387-121691)	10041 (4772-37107)	23373 (1387-121691)

16

17

18 **Supplementary Table 6: Antibodies used to stain cells for scRNAseq**

Antibody		Clone	Source	Dilution	Catalogue Number
Surface Stain					
Ex vivo dataset:					
CD3	BV510	SK7	Biolegend	1/50	344828
CD4	AF647	SK3	Biolegend	1/100	344636
CD45RA	BB515	HI100	BD Biosciences	1/400	564552
CD19	PE	H1B19	Biolegend	1/100	302208
AIM dataset:					
CD3	AF700	SK7	Biolegend	1/50	344822
CD4	PerCP Cy5.5	OKT4	Biolegend	1/50	317428
CD69	PE	FN50	Biolegend	1/50	310906
OX40	APC	ACT35	BD Biosciences	1/50	563473
Hashtags					
TotalSeq-C0251 anti-human Hashtag 1		LNH-94; 2M2	Biolegend	0.3ug/sample	394661
TotalSeq-C0252 anti-human Hashtag 2		LNH-94; 2M2	Biolegend	0.3ug/sample	394663
TotalSeq-C0253 anti-human Hashtag 3		LNH-94; 2M2	Biolegend	0.3ug/sample	394665
TotalSeq-C0254 anti-human Hashtag 4		LNH-94; 2M2	Biolegend	0.3ug/sample	394667
TotalSeq-C0255 anti-human Hashtag 5		LNH-94; 2M2	Biolegend	0.3ug/sample	394669
TotalSeq-C0256 anti-human Hashtag 6		LNH-94; 2M2	Biolegend	0.3ug/sample	394671
TotalSeq-C0257 anti-human Hashtag 7		LNH-94; 2M2	Biolegend	0.3ug/sample	394673
TotalSeq-C0258 anti-human Hashtag 8		LNH-94; 2M2	Biolegend	0.3ug/sample	394675
TotalSeq-C0259 anti-human Hashtag 9		LNH-94; 2M2	Biolegend	0.3ug/sample	394677
TotalSeq-C0260 anti-human Hashtag 10		LNH-94; 2M2	Biolegend	0.3ug/sample	394679
TotalSeq-C0296 anti-human Hashtag 11		LNH-94; 2M2	Biolegend	0.3ug/sample	328941
TotalSeq-C0262 anti-human Hashtag 12		LNH-94; 2M2	Biolegend	0.3ug/sample	394683
TotalSeq-C0263 anti-human Hashtag 13		LNH-94; 2M2	Biolegend	0.3ug/sample	394685
TotalSeq-C0264 anti-human Hashtag 14		LNH-94; 2M2	Biolegend	0.3ug/sample	394687
TotalSeq-C0265 anti-human Hashtag 15		LNH-94; 2M2	Biolegend	0.3ug/sample	394689
TotalSeq-C0276 anti-human Hashtag 16		LNH-94; 2M2	Biolegend	0.3ug/sample	394691
TotalSeq-C0277 anti-human Hashtag 17		LNH-94; 2M2	Biolegend	0.3ug/sample	394621
TotalSeq-C0277 anti-human Hashtag 18		LNH-94; 2M2	Biolegend	0.3ug/sample	394693
TotalSeq-C0279 anti-human Hashtag 19		LNH-94; 2M2	Biolegend	0.3ug/sample	394695

19

20 ***Supplementary Figures***

21

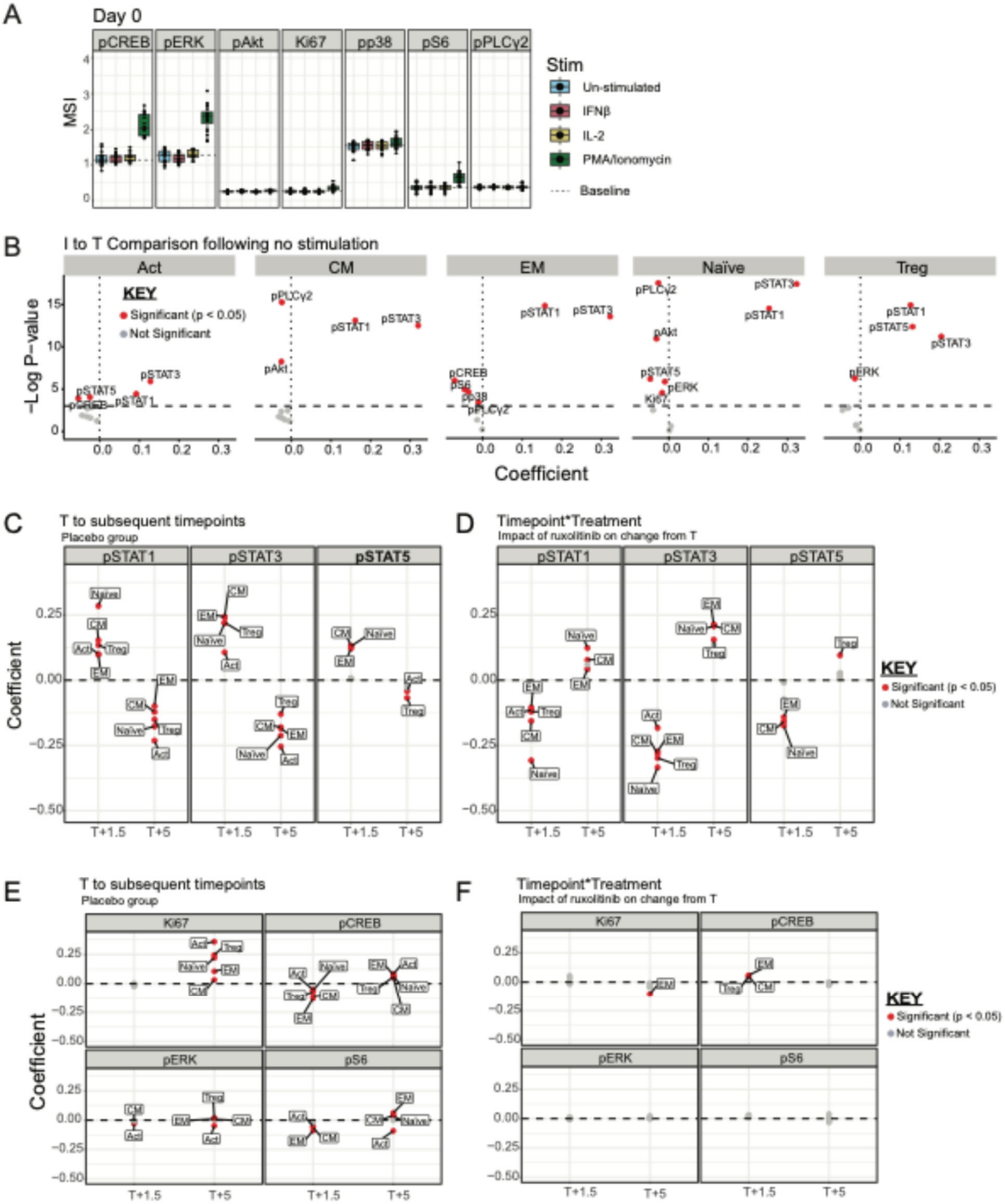

22

23

24

25 ***Supplementary Figure 1: Analysis of phosphoproteins in CD4 T cells during malaria.***
26 ***A***. *Mean Signal Intensity (MSI) of phosphorylated proteins in CD4+ T cells following*
27 *stimulation of whole blood with PBS (un-stimulated condition), IFNβ, IL-2 and PMA/Ionomycin*
28 *at the pre-inoculation (baseline) time point for 15 minutes. The box plots show the extent of the*
29 *lower and upper quartiles and the median, while each point represents a study participant*
30 *(n=20).* ***B.*** *Volcano Plots showing the coefficient and p values of mixed model analysis of the*
31 *effect of infection (pre-treatment time point (T, day 8/9) compared to inoculation time point*
32 *(I, day 0)), on the mean signal intensity (MSI) of the phosphorylated proteins and Ki67 in CD4+*
33 *T cell subsets in unstimulated cells. Proteins with a significant change are in red.* ***C-F.***
34 *Coefficient from mixed effect models analysing MSI for phosphoproteins in unstimulated cells in*
35 *indicated CD4 T cell subset, analysing changes with time (**C/E**), comparing T with T+1.5 and*
36 *T+5 and for the interaction between timepoint and treatment (**D/F**). Coefficient is indicated for*
37 *each subset and timepoint, with significant changes in red. Related to Figure 1*
38
39

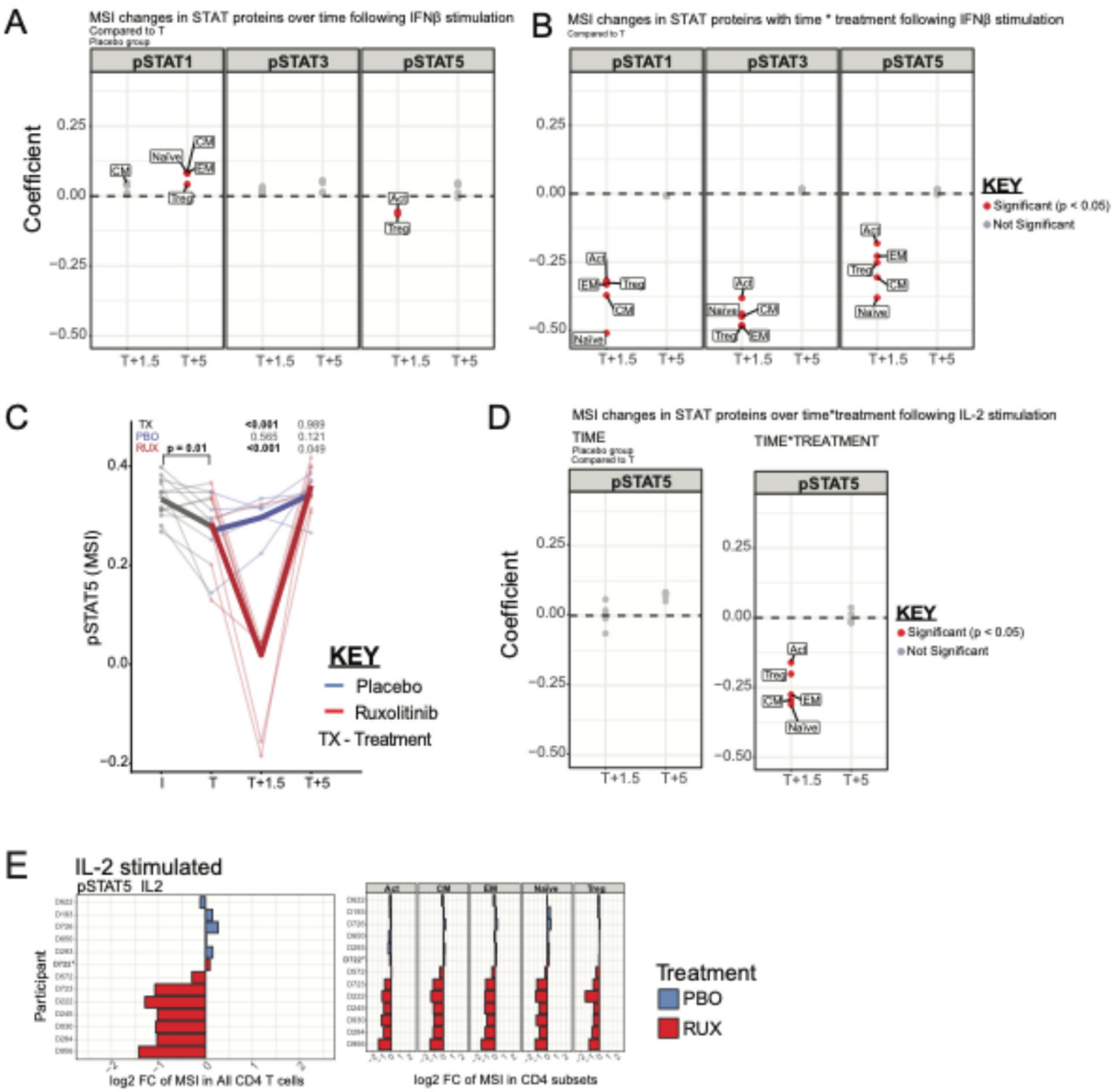

Supplementary Figure 2: pSTATs in CD4 T cells during malaria following IFNβ and IL-2 stimulations.

A) *Coefficient from mixed effect models analysing MSI for phosphoproteins in cells stimulated with IFNβ in indicated CD4 T cell subset, analysing changes with time (**A**) comparing T with T+1.5 and T+5 and for the interaction between timepoint and treatment (**B**). Coefficient is indicated for each subset and timepoint, with significant changes in red. **C)** pSTAT5 expression in*

CD4 T cells at I, T, T+1, T+5 in IL-2 stimulated cultures. Data are log transformed median signalling intensity, with thin lines representing each participant and coloured by treatment group. Prior to randomisation data are in grey; following randomisation ruxolitinib-treated participants are red and placebo-treated are blue. TX is p values for the interaction term between each timepoint (compared to T) and treatment groups. p values for the comparison between each timepoint and T are shown for the placebo (PBO) and ruxolitinib (RUX) groups, and were determined from contrasts. ***D)*** *Coefficient from mixed effect models analysing MSI for pSTAT5 in cells stimulated with IL-2 in indicated CD4 T cell subset, analysing changes with time comparing T with T+1.5 and T+5 and for the interaction between timepoint and treatment. Significant changes are indicated in red.* ***E)*** *Fold change between T and T+1.5 expression of pSTAT5 in total CD4 T cells and CD4 T cell subsets for IL-2 stimulated cells. Data for each participant are shown. Related to Figure 1*

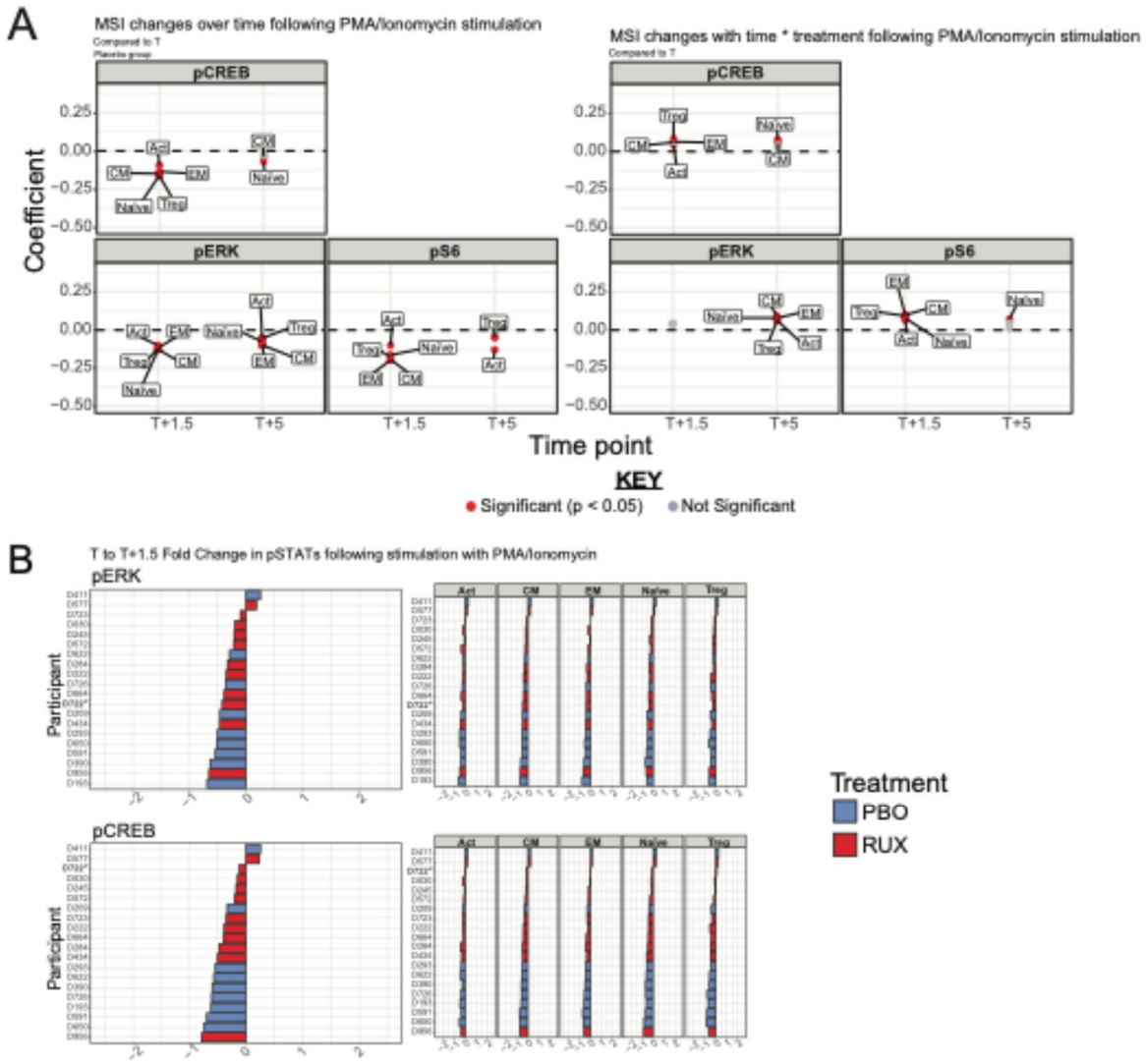

Supplementary Figure 3: Phosphorylation of proteins in PMA stimulated cultures in CD4 T cells during malaria.

A) *Coefficient from mixed effect models analysing MSI for pCREB, pERK and pS6 in cells stimulated with PMA/Ion in indicated CD4 T cell subset, analysing changes with time comparing T with T+1.5 and T+5 and for the interaction between timepoint and treatment. Significant changes are indicated in red.* ***B)*** *Fold change between T and T+1.5 expression of pERK and pCREB in total CD4 T cells and CD4 T cell subsets for PMA/Ion stimulated cells. Data for each participant are shown. Related to Figure 1*

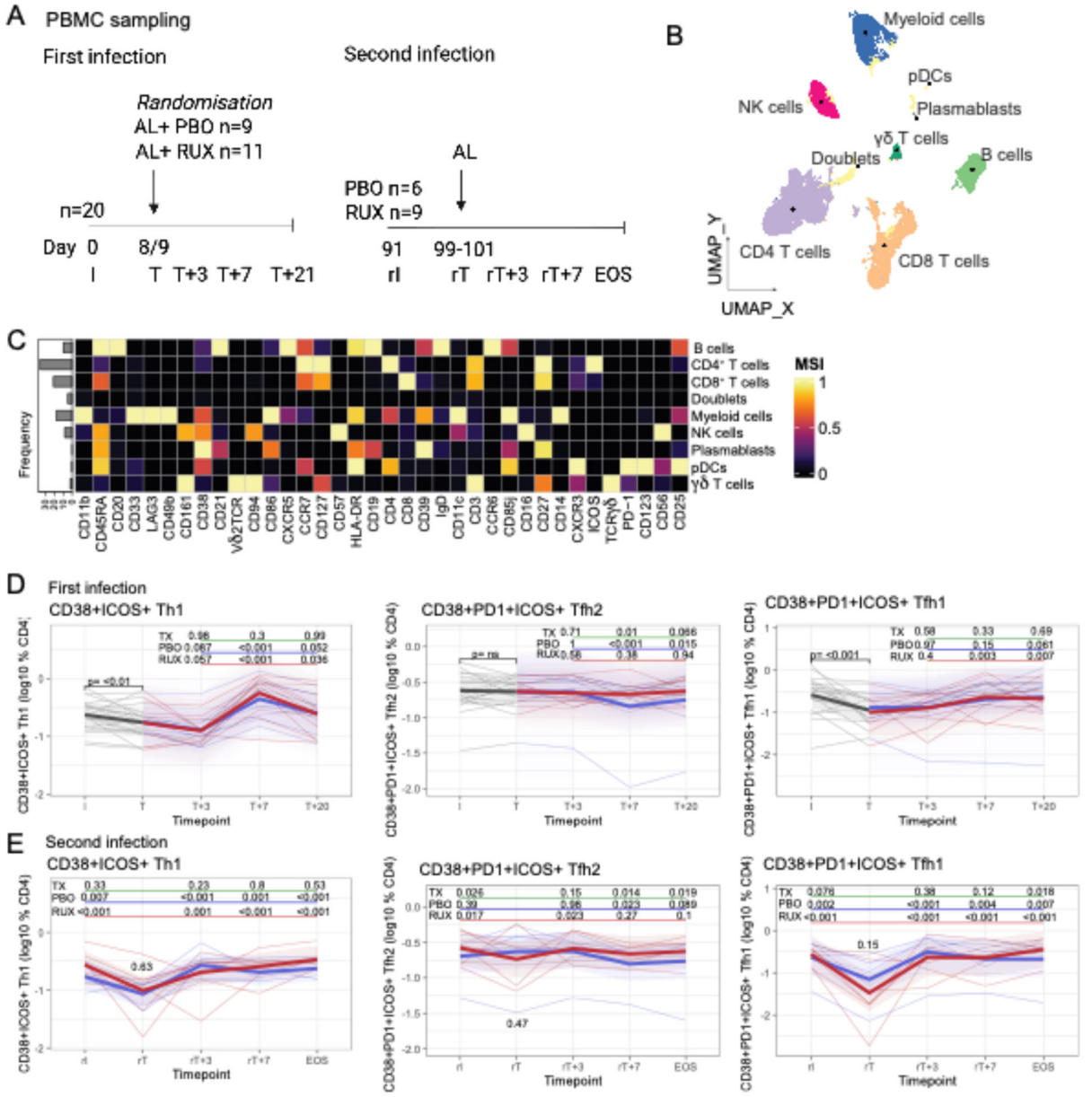

Supplementary Figure 4: CD4 T cell frequencies and activation

A) *PBMCs were collected at 5 time points in first and second infection. *one participant in the Rux group in second infection tested positive for COVID-19 and received malaria treatment early.* ***B/C)*** *PBMCs were analysed by CyTOF and CD4 T cells identified for further analysis.* ***D/E)*** *CD38+ICOS+ Th1, and CD38+PD1+ICOS+ Tfh2 and Tfh1 CD4 T cells in first and second infection. Data are log10 frequencies of CD4 T cells, with thin lines representing each participant. Prior to randomisation data are in grey, following randomisation ruxolitinib-treated participants are in red and placebo-treated are in blue. P values are from linear mixed effect models, with bold lines representing the mean of the predicted values from the fitted models for each group. TX is p values for the interaction term between each timepoint (compared to T) and treatment groups (underlined in green). P values for the comparison between each timepoint and*

85 *T are shown for the placebo (PBO, underlined in blue) and ruxolitinib (RUX, underlined in red)*
86 *groups, and were determined from contrasts. Related to Figure 2.*

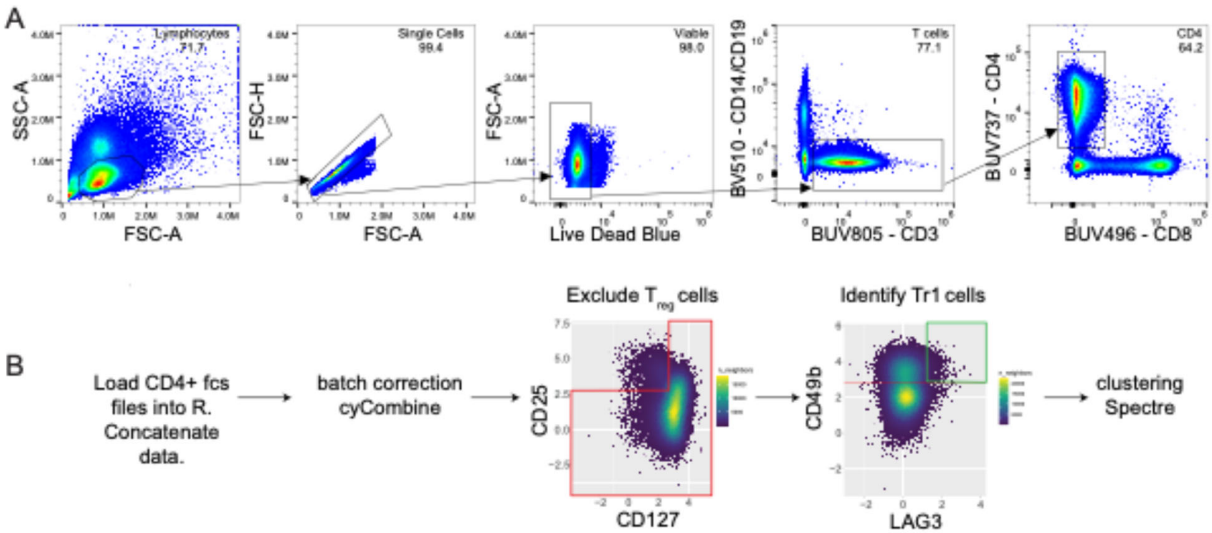

Supplementary Figure 5: Tr1 cell analysis strategy

A) *CD4+ T cells were identified based on FSC/SSC, live/dead staining, CD14-CD19-/CD3+, CD4+ cells.* ***B)*** *CD4+ cells were exported after gating and analysed in R. Batch correction was performed in cyCombine, Treg cells removed (CD25+CD127low), and Tr1 cells identified based on LAG3+CD49b+. Related to Figure 3.*

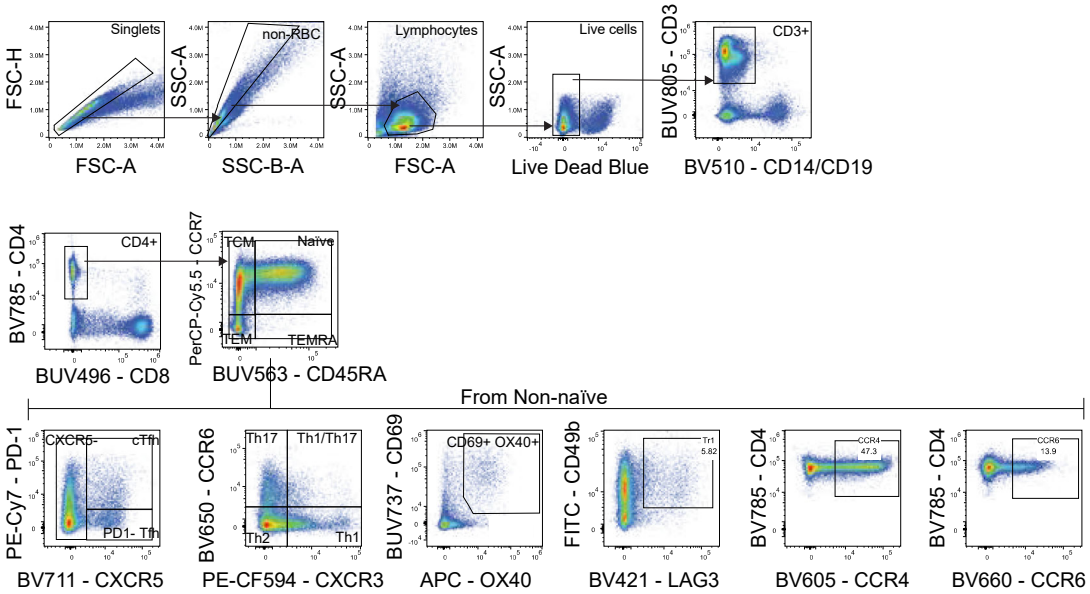

Supplementary Figure 6: Gating Strategy employed to identify the AIM+ CD4^{+} T cell populations

After gating for the CD45RA^{+} CCR7^{+} naive cells, a "not" gate was used to remove this population and the other CD4^{+} T cell subsets were identified from the non-naive CD4+ T cells. Following this, Boolean gating was using to examine AIM^{+} CD4^{+} T cells. Figure represents PBMCs from Day 15 for D726 in the Placebo group following 18 hour culture with parasitised red blood cells. AND gates were set to analyse all AIM^{+} cells and subset. Related to Figure 4.

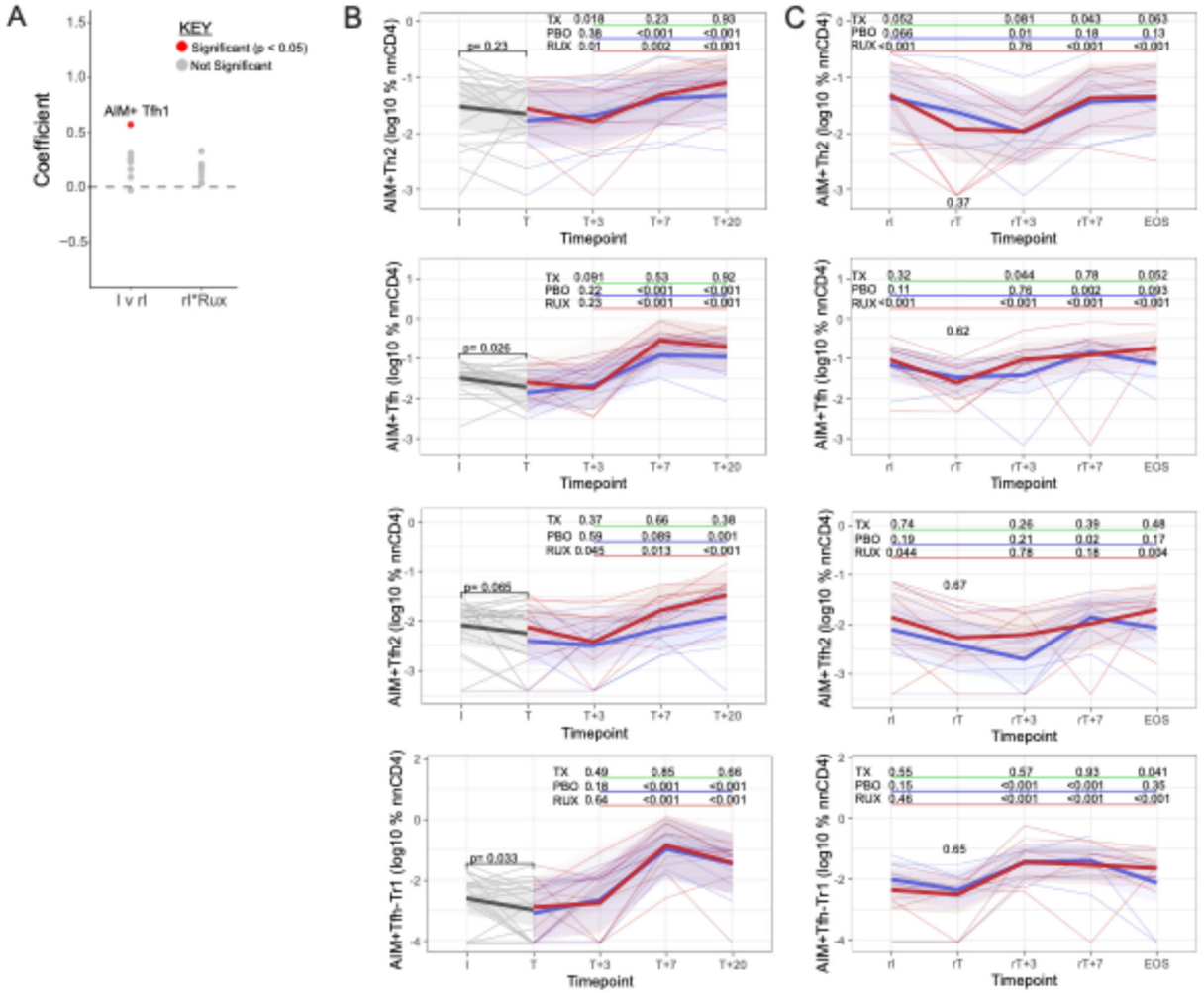

Supplementary Figure 7: AIM+ CD4 T cell response during first and second infection
Parasite specific CD4 T cells were identified using Activation Induced Marker assay at inoculation (I), treatment (T) and post treatment timepoints (T+3, T+7 and T+20) in first infection, and at re-inoculation (rI), re-treatment (rT) and post treatment timepoints (rT+3, rT+7, EOS) in second infection. ***A.*** *Coefficient of linear mixed models comparing first to second infection inoculation (I verse rI) interaction term of ruxolitinib treatment group. Only AIM+ Tfh1 cells were elevated at rI, and this was not impacted by ruxolitinib.* ***B/C)*** *AIM+ Th2, AIM+ Tfh (total Tfh) and AIM+ Tfh2, and AIM+Tfh-Tr1 cells in first and second infection. Data are log10 frequencies of malaria specific AIM+ CD4 T cells, with thin lines representing each participant. Prior to randomisation is in grey, following randomisation ruxolitinib-treated participants are red and placebo are blue. P values are from linear mixed effect models, with bold lines representing the mean of the predicted values from the fitted models for each group. TX is p values for the interaction term between each timepoint (compared to T) and treatment groups (underlined in green). P values for the comparison between each timepoint and T are shown for the placebo (PBO, underlined in blue) and ruxolitinib (RUX, underlined in red) groups, which were determined from contrasts. P value for the difference at rT between placebo and ruxolitinib group, calculated from the intercept is shown at rT.*

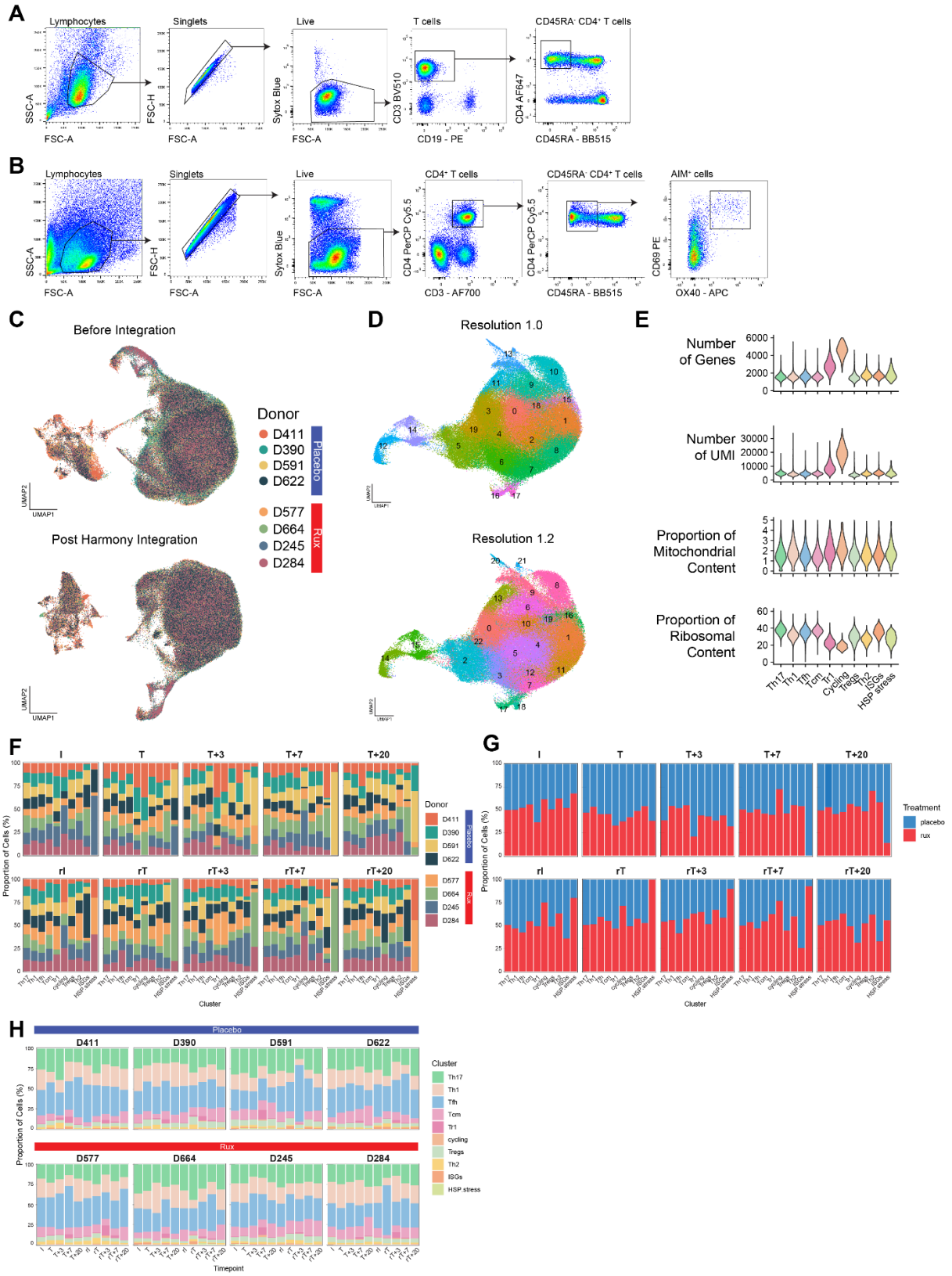
A
Lymphocytes
Singlets
Live
T cells
CD45RA⁻ CD4⁺ T cells
SSC-A
FSC-A
FSC-H
Sytox Blue
CD3 BV510
CD19 - PE
CD4 AF647
CD45RA - BB515
B
CD4⁺ T cells
AIM⁺ cells
CD4 PerCP Cy5.5
CD3 - AF700
CD69 PE
OX40 - APC
C
Before Integration
Post Harmony Integration
UMAP1
UMAP2
Donor
D411
D390
D591
D622
Placebo
D577
D664
D245
D284
Rux
D
Resolution 1.0
Resolution 1.2
E
Number of Genes
Number of UMI
Proportion of Mitochondrial Content
Proportion of Ribosomal Content
Th17
Th1
Tfh
Tcm
Tr1
Cycling
Tregs
Th2
ISGs
HSP stress
F
I
T
T+3
T+7
T+20
rI
rT
rT+3
rT+7
rT+20
Proportion of Cells (%)
Cluster
G
Treatment
placebo
rux
H
Timepoint

123

124 ***Supplementary Figure 8: scRNAseq analysis of CD4$^+$ T cell responses during first and second***
125 ***infection. A)*** *Flow cytometry gating strategy for isolating ex vivo antigen experienced (CD45RA$^-$*
126 *) CD4$^+$ T cells and* ***B)*** *AIM$^+$ (CD69$^+$OX40$^+$) CD4$^+$ T cells.* ***C)*** *UMAP visualisation of ex vivo*
127 *and AIM$^+$ CD4$^+$ T cells coloured by donor prior to and post-Harmony integration by donor.* ***D)***
128 *UMAP visualisation showing clustering of the ex vivo CD4$^+$ T cells at resolution 1 and 1.2.* ***E)***
129 *Violin plots showing quality control metrics for the ex vivo CD4$^+$ T cells.* ***F)*** *Stacked bar graphs*
130 *split by timepoint showing the proportion of donor or* ***G)*** *treatment group per ex vivo CD4$^+$ T*
131 *cell cluster.* ***H)*** *Stacked bar graphs split by donor showing the proportion of ex vivo CD4+ T*
132 *cell cluster per timepoint.*

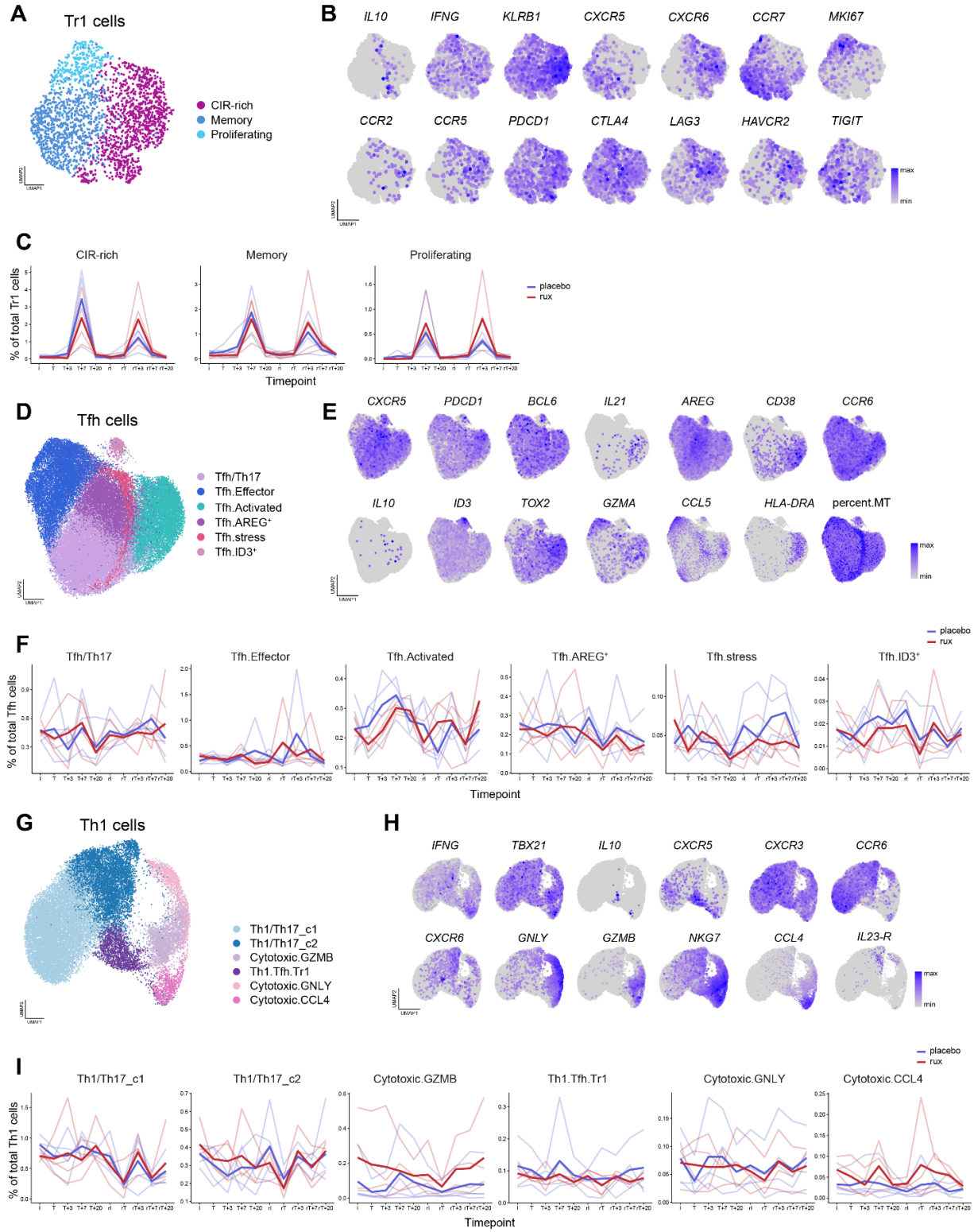
A
Tr1 cells
CIR-rich
Memory
Proliferating
B
IL10
IFNG
KLRB1
CXCR5
CXCR6
CCR7
MKI67
CCR2
CCR5
PDCD1
CTLA4
LAG3
HAVCR2
TIGIT
max
min
C
CIR-rich
Memory
Proliferating
% of total Tr1 cells
placebo
rux
Timepoint
D
Tfh cells
Tfh/Th17
Tfh.Effector
Tfh.Activated
Tfh.AREG+
Tfh.stress
Tfh.ID3+
E
CXCR5
PDCD1
BCL6
IL21
AREG
CD38
CCR6
IL10
ID3
TOX2
GZMA
CCL5
HLA-DRA
percent.MT
max
min
F
Tfh/Th17
Tfh.Effector
Tfh.Activated
Tfh.AREG+
Tfh.stress
Tfh.ID3+
% of total Tfh cells
placebo
rux
Timepoint
G
Th1 cells
Th1/Th17_c1
Th1/Th17_c2
Cytotoxic.GZMB
Th1.Tfh.Tr1
Cytotoxic.GNLY
Cytotoxic.CCL4
H
IFNG
TBX21
IL10
CXCR5
CXCR3
CCR6
CXCR6
GNLY
GZMB
NKG7
CCL4
IL23-R
max
min
I
Th1/Th17_c1
Th1/Th17_c2
Cytotoxic.GZMB
Th1.Tfh.Tr1
Cytotoxic.GNLY
Cytotoxic.CCL4
% of total Th1 cells
placebo
rux
Timepoint

136 ***Supplementary Figure 9: scRNAseq Th1-Tfh-Tr1 axis cells re-clustering.***
137 ***A)*** *UMAP visualisation shows three clusters of Tr1 cells after subsetting and re-clustering and*
138 ***B)*** *expression of select cluster marker genes.* ***C)*** *Line graphs showing the cluster frequency as a*
139 *percentage of total Tr1 cells during first and second infections. Lines are coloured by treatment*
140 *group, with bold lines representing group means and transparent lines showing frequencies for*
141 *each participant.* ***D)*** *UMAP visualisation shows six clusters of Tfh cells after subsetting and re-*
142 *clustering and* ***E)*** *expression of select cluster marker genes.* ***F)*** *Line graphs showing the cluster*
143 *frequency as a percentage of total Tfh cells during first and second infections. Lines are*
144 *coloured by treatment group, with bold lines representing group means and transparent lines*
145 *showing frequencies for each participant.* ***G)*** *UMAP visualisation shows six clusters of Th1 cells*
146 *after subsetting and re-clustering and* ***H)*** *expression of select cluster marker genes.* ***I)*** *Line*
147 *graphs showing the cluster frequency as a percentage of total Th1 cells during first and second*
148 *infections. Lines are coloured by treatment group, with bold lines representing group means and*
149 *transparent lines showing frequencies for each participant.*
150
151
152

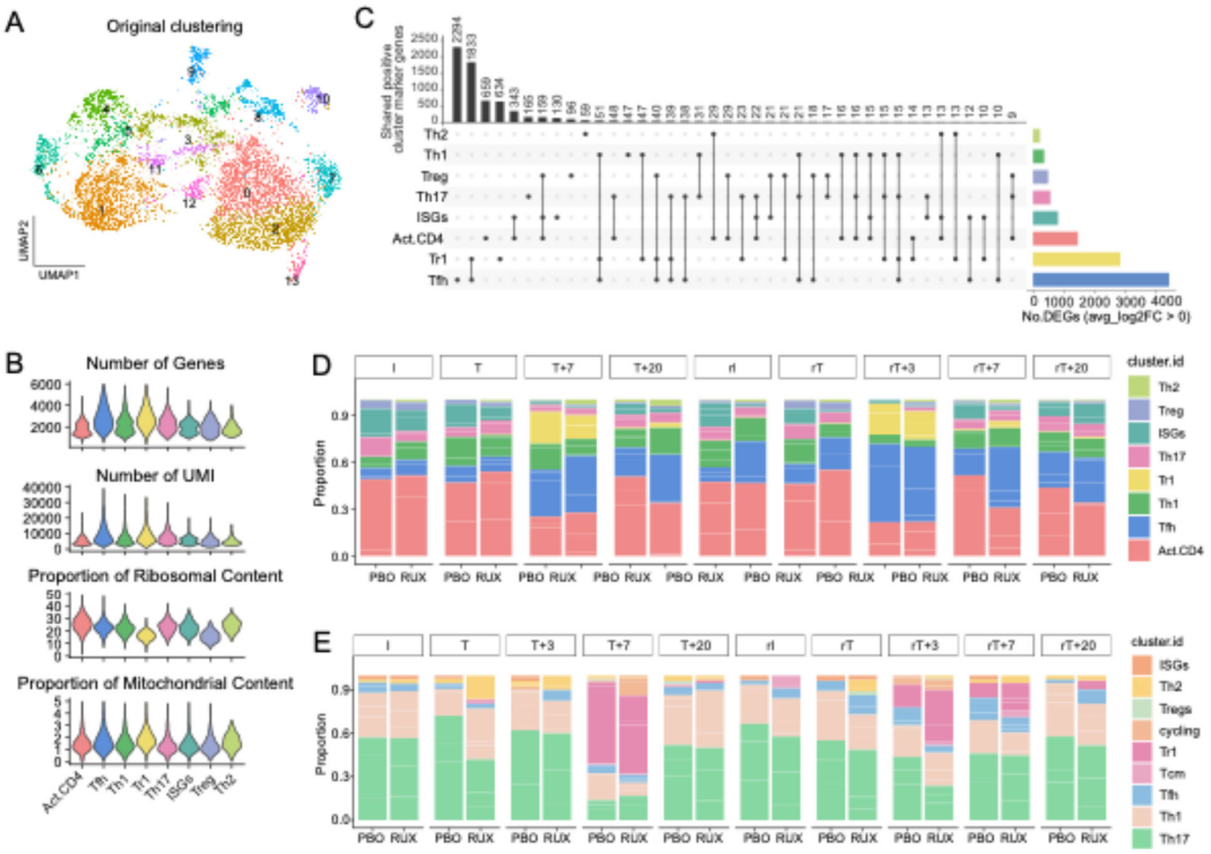

Supplementary Figure 10: AIM+ scRNAseq data and malaria specific cells.

__A)__ UMAP visualisation showing clustering of the AIM+ CD4^{+} T cells. __B)__ Violin plots showing quality control metrics for the AIM+ CD4^{+} T cells. __C)__ Upset plot showing the number of shared marker genes between clusters in AIM+ data set. The bar graph on the right shows the total number of differentially expressed cluster marker genes for each subset. __D)__ Subset proportions of AIM+ CD4 T cells at each timepoint, by treatment group. __E)__ Subset proportions of malaria-specific cells identified within ex vivo data set based on TCR analysis of AIM+ data set.